

www.acsaem.org Article

Iridium-Based Materials as an Electrocatalyst in Computational Investigation of Their Performance for Hydrogen and Oxygen **Evolution Reactions**

Marionir M. C. B. Neto, Pedro Ivo R. Moraes, and Juarez L. F. Da Silva*



Cite This: https://doi.org/10.1021/acsaem.5c02853



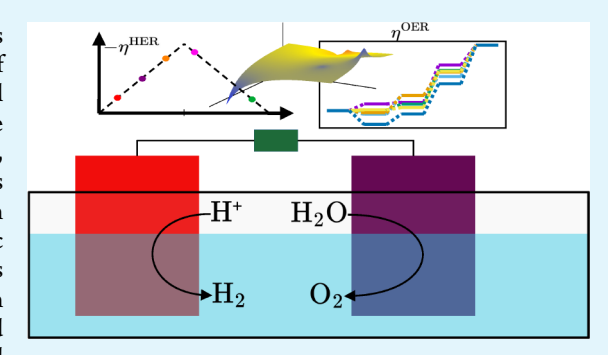
ACCESS I

III Metrics & More

Article Recommendations

s Supporting Information

ABSTRACT: Electrocatalytic water splitting, a process that converts water into hydrogen and oxygen, underpins the development of sustainable and carbon-neutral energy systems. Despite substantial progress, there remains an incomplete atomistic understanding of the mechanisms by which noble-metal catalysts lower reaction overpotentials, thus hampering the rational design of cost-effective alternatives. In this study, we use density functional theory calculations in combination with the computational hydrogen electrode model to explore the catalytic properties of metallic iridium and its oxides (IrO₂ and Ir₂O₃) on various crystallographic surfaces concerning the hydrogen and oxygen evolution reactions. The analysis indicates that variations in the oxidation state and surface coordination profoundly influence the adsorption energetics and



catalytic efficacy. Among the investigated systems, IrO2 surfaces exhibit optimal adsorption energies for oxygen evolution intermediates, resulting in low overpotentials while maintaining moderate hydrogen evolution activity. In contrast, metallic Ir and Ir₂O₃(0001) facets display hydrogen evolution reaction activity comparable with pure Ir, yet their oxygen evolution reaction performance is hampered by the excessive stabilization of intermediates. The $Ir_2O_3(1010)$ surface binds intermediates too strongly, leading to suboptimal activity for both reactions. Additionally, the preferred adsorption sites and charge-transfer characteristics are seen to vary significantly with surface termination, directly affecting the thermodynamics of intermediate formation. Together, these findings elucidate the interaction between surface structure, oxidation state, and electronic properties in dictating the electrocatalytic performance of iridium-based materials, providing valuable insights into the rational design of advanced catalysts for water splitting. KEYWORDS: iridium metal, iridium oxides, water splitting, hydrogen evolution reaction, oxygen evolution reaction

1. INTRODUCTION

Hydrogen (H₂) serves as a fundamental industrial commodity with extensive applications across various technological domains, including the synthesis of ammonia, methanol production, petroleum refining, and used in advancement energy conversion systems such as fuel cells. Despite its extensive applicability, the majority of industrial H₂ is currently synthesized through steam methane reforming, a process that produces considerable CO₂ emissions and maintains a significant reliance on fossil fuels.² This carbon-intensive pathway highlights the urgent need to transition toward more environmentally sustainable hydrogen production techniques.

In this regard, the production of renewable, or green, H2 via electrolysis of water powered by renewable energy sources has emerged as a highly promising alternative. The inherent versatility of green H₂ hydrogen positions it as an essential energy carrier in global efforts toward decarbonization, capable of directly substituting H2 derived from fossil fuels or being converted into valuable chemical derivatives such as green methanol and ammonia. Furthermore, through sector coupling, where green hydrogen (H₂) and its derivatives

function as intermediaries, this methodology facilitates the efficient integration of renewable energy sources, particularly solar and wind energy, thus improving the flexibility of the system and promoting a sustainable circular energy infrastructure.3,4

Water splitting involves two critical half-reactions: the hydrogen evolution reaction (HER) and the oxygen evolution reaction (OER).5 However, the predominant challenge to their extensive practical application is the high overpotentials associated with these fundamental reactions, thus requiring the discovery and optimization of highly efficient catalysts. Noble metals currently dominate the sphere of electrocatalytic performance, despite their substantial costs. Their superior

Received: September 15, 2025 Revised: November 1, 2025 Accepted: November 3, 2025



intrinsic activity, stability across an extensive pH spectrum, and considerable durability make them the preferred materials for rigorous industrial applications. Specifically, platinum (Pt) is widely acknowledged as the exemplary catalyst for HER, while ruthenium dioxide (RuO₂) and iridium dioxide (IrO₂) are the standards for OER, with IrO₂ being particularly celebrated for its exceptional stability under strenuous OER conditions. Furthermore, Ir has drawn increasing interest due to its favorable electronic structure, high corrosion resistance, and excellent electrical conductivity, all of which contribute to its robust performance in electrochemical contexts. 10,11

Substantial research efforts have been directed toward the exploration of Ir-based materials for electrocatalysis, yielding significant insights into their behavior. For example, empirical studies have shown that metallic Ir has higher catalytic activity compared to rutile-like IrO₂ in certain reactions, ^{11,12} a phenomenon often attributed to its lower *d*-band center, which directly affects the binding strength of adsorbates. ¹³ In its oxide forms, the strongest binding energy is specifically attributed to the Ir³⁺ centers. ¹⁴

However, despite these valuable insights, a notable limitation remains: computational investigations of the electrocatalytic performance of Ir₂O₃ are surprisingly sparse. This represents a significant research gap, particularly as α -Ir₂O₃, although generally deemed less stable than IrO2, has been reported to exhibit crucial p-type conductivity in its corundum-like morphology, 15 a property of considerable interest for various energy storage and catalytic applications. Moreover, the successful experimental synthesis of this compound 16 further highlights its practical importance. Additionally, α -Ir₂O₃ provides a semiconducting system that contrasts with metallic Ir and conductive IrO2, allowing a more comprehensive investigation of how different electronic structures and oxidation states influence electrocatalytic performance. Consequently, a fundamental computational understanding of the distinct behaviors of Ir across its metallic and oxide states (Ir⁰, Ir4+, and Ir3+) is essential for the rational design of nextgeneration catalysts.

This study explicitly addresses the identified gap by using theoretical methods to investigate the fundamental electronic and energetic properties that differentiate metallic iridium surfaces from their oxides in various oxidation states. We perform computational analyzes on metallic Ir, IrO₂, and Ir₂O₃ employing density functional theory (DFT) calculations combined with the computational model of hydrogen electrodes. Through this approach, we strive to provide a comprehensive comparative understanding of how the oxidation state and the local coordination environment intricately affect their intrinsic properties relevant to electrocatalysis. 17 Based on the DFT framework, we provide robust comparative insights, extending beyond traditional correlations to integrate thermodynamic perspectives with a comprehensive analysis of electronic and structural properties, thus offering a deeper understanding of catalytic performance across various iridium phases.

2. THEORETICAL APPROACH AND COMPUTATIONAL DETAILS

2.1. Total Energy Calculations. Our spin-polarized calculations were performed using the DFT framework implemented in the Vienna Simulation Package (VASP), version 5.4.4, ^{18,19} which employs the projector augmentedwave (PAW) method ^{19,20} to describe the interaction between

the core and the valence electrons. For the exchange-correlation (XC) energy functional, we applied the Perdew–Burke–Ernzerhof (PBE) formulation, ²¹ recognized as one of the most used approximations for the XC functional. To improve the description of interactions between molecular species and substrates, ^{22,23} which constitutes the primary objective of this study, we integrated conventional DFT-PBE with the semiempirical D3 van der Waals (vdW) correction, thus improving the description of long-range vdW interactions. ²⁴

The equilibrium lattice parameters of bulk iridium (Ir) in the face-centered cubic (fcc) phase, along with those of rutile-type IrO2 and corundum-structured $\alpha\text{-Ir}_2\text{O}_3$, were obtained through full structural relaxations involving the simultaneous minimization of atomic forces and the stress tensor. To ensure robust convergence of total energies, the plane wave cutoff energies of 639.686 eV for fcc Ir and 868.862 eV were employed for both IrO2 and Ir2O3. These values correspond to twice the maximum recommended cutoff thresholds for iridium and oxygen, as provided in the associated POTCAR files, thereby offering enhanced accuracy and numerical stability. For the Brillouin zone integration, Monkhorst–Pack² k-point grids of $18\times18\times18$, $4\times4\times6$, and $5\times5\times5$ were used for fcc Ir, rutile IrO2 and $\alpha\text{-Ir}_2\text{O}_3$, respectively.

The calculations for both clean slabs and molecules adsorbed on these slabs were performed using a plane wave cutoff energy of 488.734 eV, which exceeds the highest recommended ENMAX value by 12.5% among the chemical species considered in this study. The slabs were designed with a vacuum region spacing of 15 Å, which is required to minimize the interactions between repeated slabs (periodic boundary conditions). The following surface unit cells were selected: $Ir(111)-(2\times 2)$, $Ir(100)-(2\times 2)$, $IrO_2(110)-(1\times 2)$ 2), $IrO_2(100)-(2 \times 2)$, $\alpha -Ir_2O_3(0001)-(1 \times 2)$, and α - $Ir_2O_3(10\overline{10})-(2\times 1)$. The k-point meshes were designated at $9 \times 9 \times 1$ for metallic Ir, $3 \times 3 \times 1$ for IrO₂, and $5 \times 5 \times 1$ for α-Ir₂O₃. The dimensions of the slabs and the thickness of the vacuum were validated using adsorption convergence tests using H and OH in Ir(111), as elaborated in the electronic Supporting Information.

The vibrational frequencies of the adsorbates were calculated via finite differences using the second derivative method. Gas-phase species were modeled using a 20.00 \times 20.25 \times 20.50 Å orthorhombic box, sampled at the Γ -point (1 \times 1 \times 1), ensuring negligible electronic dispersion effects. The convergence criteria were established at 10^{-6} eV for the total energy and 0.01 eV Å $^{-1}$ for the atomic forces in all atoms.

2.2. Computational Hydrogen Electrode Model. The computational hydrogen electrode (CHE) model^{26,27} uses the reversible hydrogen electrode (RHE) as a reference to simulate applied potentials (U). In this framework, the electrochemical potential of a proton–electron pair refers to the standard hydrogen electrode (SHE), which is defined by the equilibrium of the half-cell. Thus, we have the following equation,

$$\frac{1}{2}H_2 \rightleftharpoons H^+ + e^- \tag{1}$$

which is in equilibrium under any pH and temperature conditions when U=0 V. The applied potential is incorporated into the expression of the free energy linked to eq 1. $G_{\text{H}^++e^-}=G_{\text{H}_2}-eU$, where e is the elementary charge of the electron. The onset potential is determined by the potential determining step (PDS), described by the following

expression $U_{\rm onset} = \frac{\Delta G_{\rm PDS}}{e}$. Thus, the overpotential (η) is defined as the difference between the onset potential and the standard equilibrium potential of any reaction, $U_{\rm eq}$,

$$\eta = |U_{\text{onset}} - U_{\text{eq}}| \tag{2}$$

The Gibbs free energy for each reaction configuration is expressed by the following equation,

$$G = E_{\text{tot}} + ZPE + \int C_p dT - TS$$
(3)

where $E_{\rm tot}$ is the DFT total energy. The zero-point energy (ZPE), the enthalpic correction ($\int C_p dT$) and the entropic correction (-TS) are derived from vibrational frequency calculations of the adsorbed intermediates. These energy contributions are calculated at 298.15 K under the harmonic approximation using the thermochemistry module as implemented in the Atomic Simulation Environment (ASE) package. The respective relations are the following,

$$ZPE = \sum_{i} \frac{1}{2} \epsilon_{i}$$
 (4)

$$\int C_p dT = \sum_i \frac{\epsilon_i}{e^{\epsilon_i/k_B T} - 1}$$
(5)

and

$$S = k_{\rm B} \sum_{i} \frac{\epsilon_{i}}{k_{\rm B} T (e^{\epsilon_{i}/k_{\rm B}T} - 1)} - \ln(1 - e^{\epsilon_{i}/k_{\rm B}T})$$
(6)

Here, ϵ_i are the energies of the vibrational mode, $k_{\rm B}$ is the Boltzmann constant, and T is the temperature. ΔG values represent relative values, with the reference always being the value of G of the reactant state. Solvation effects were not included in this study, as our objective is to comparatively analyze the intrinsic thermodynamic properties of the intermediates, whose qualitative trends are preserved even without explicit consideration of solvation. ²⁹

2.2.1. Hydrogen Evolution Reaction. The cathodic half-cell of water splitting has been extensively studied, primarily focusing on the HER:

$$H^+ + e^- \to \frac{1}{2} H_2 \tag{7}$$

There are two reaction steps for HER,

$$H^+ + e^- + * \to H^*$$
 (8)

and

$$H^* \to \frac{1}{2}H_2 + *$$
 (9)

Its standard reduction potential is $U_{\rm eq}=0$ V versus RHE and involves two elementary steps: adsorption and intermediate desorption, as shown in Figure 1. These steps correspond to two proton-coupled electron transfer (PCET) processes: adsorption and desorption. The key reaction intermediate H*, where * denotes a substrate site, is central to thermodynamic analysis. For HER, the values of ΔG refer to the state of H⁺ + *. According to Sabatier's principle, 30 a positive $\Delta G_{\rm H}$ indicates weak hydrogen adsorption, identifying the adsorption step as the PDS. For HER, the values of ΔG refer to the state of H + *. In contrast, a negative $\Delta G_{\rm H^*}$ reflects strong hydrogen adsorption, making the desorption PDS. For an ideal catalyst, $\Delta G_{\rm H^*}=0$. Regardless of whether adsorption

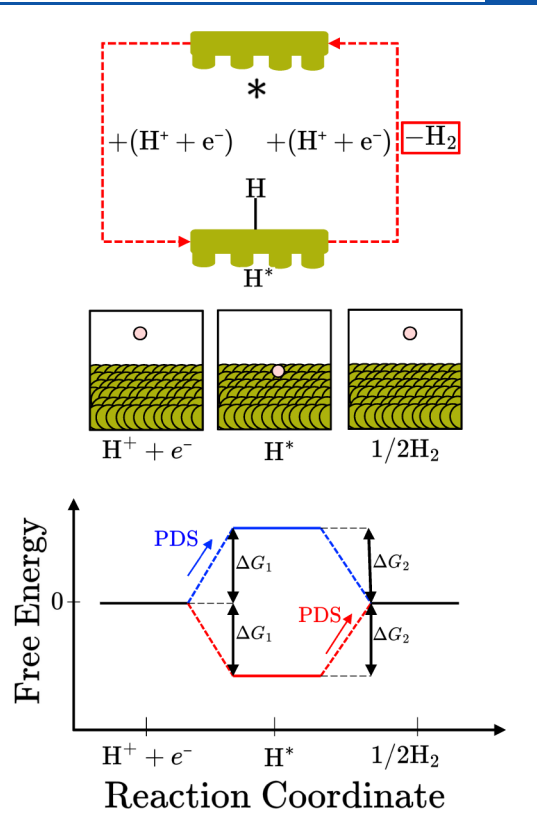


Figure 1. Schematic representation of the HER. Top panel: Proton-coupled electron-transfer mechanisms. Middle panel: Computational setup employed for the computational modeling. Bottom panel: Gibbs free-energy diagram describing the HER pathway and associated energetics.

or desorption is PDS, the magnitude of its change in free energy is equal to $|\Delta G_{H^*}|$, since the reactants and products of the overall reaction share the same energy level. Consequently, the variation in the free energy of PDS can be expressed as $\Delta G_{\text{PDS}} = |\Delta G_{H^*}|$. Therefore, eq 2 simplifies for the HER case, becoming dependent on only one thermodynamic parameter,

$$\eta^{\text{HER}} = \frac{|\Delta G_{\text{H}}^*|}{e} \tag{10}$$

2.2.2. Oxygen Evolution Reaction. For acidic media, Nørskov et al.²⁶ developed a thermodynamic framework to model the description of the OER. The anodic reaction is typically the primary bottleneck in the water splitting process, significantly limiting its efficiency.^{31,32} The adsorbate evolution mechanism is the conventional and widely accepted approach,³³ involving four PCET steps, as illustrated in Figure 2. The overall reaction is given by

$$2H_2O \rightarrow O_2 + 4H^+ + 4e^-$$
 (11)

with a standard potential (T=298.15K, pH = 0 and p=1 bar) versus RHE of $U_{\rm eq}=1.23$ V, resulting in a Gibbs free energy change of $\Delta G=4.92$ eV, where ΔG values are referenced to the $2{\rm H}_2{\rm O}$ + * state, as determined by the relationship $\Delta G=-nFU_{\rm eq}$, where n=4 is the number of electrons involved in the reaction, and F is the Faraday constant. Thermodynamic descriptions of ${\rm O}_2$ in DFT often exhibit discrepancies and deviate from experimental values. Until a correlation-exchange functional capable of correcting these effects becomes available, the overall reaction equation is semiempirically

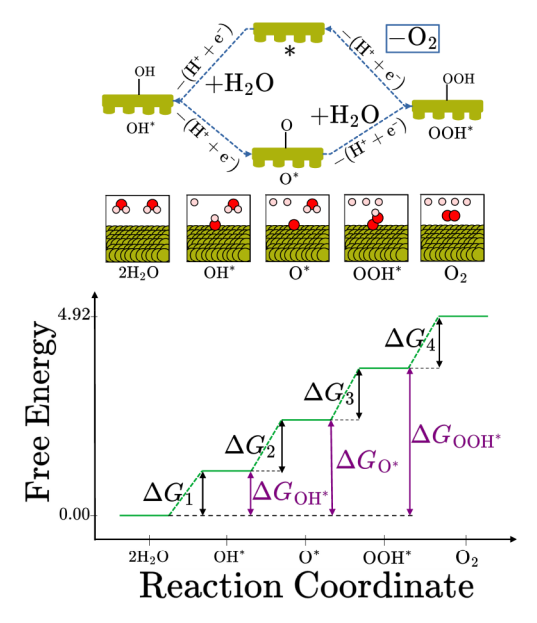


Figure 2. Schematic representation of the OER. Top panel: Proton-coupled electron-transfer steps involved in the OER. Middle panel: Computational setup employed for modeling the OER. Bottom panel: Gibbs free-energy diagram describing the OER pathway and its associated energetics.

employed to determine its Gibbs free energy as $G_{\rm O_2}$ = 4.92 – $2 \cdot G_{\rm H,O}$.³⁴

For each of the four intermediate reactions,

$$H_2O_{(l)} + * \rightarrow OH^* + H^+ + e^- \qquad \Delta G_1$$
 (12)

$$OH^* \to O^* + H^+ + e^- \qquad \Delta G_2$$
 (13)

$$H_2O_{(l)} + O^* \to OOH^* + H^+ + e^- \qquad \Delta G_3$$
 (14)

and

$$OOH^* \to O_2 + * + H^+ + e^- \qquad \Delta G_4$$
 (15)

The Gibbs free energy is determined for the four intermediate reactions (ΔG_1 , ΔG_2 , ΔG_3 , and ΔG_4), and the highest value among them is considered $\Delta G_{\rm PDS} = \max(\Delta G_1, \Delta G_2, \Delta G_3, \Delta G_4)$, with the corresponding step classified as PDS. This methodology can be applied at an arbitrary pH, as both alkaline and acidic media show the same reference at RHE. A correction factor of $K_{\rm B} \cdot T \cdot {\rm pH}$ should be applied, where $K_{\rm B}$ represents the Boltzmann constant. This correction leads to zero at pH = 0. In other cases, the standard equilibrium potential, $U_{\rm eq}$, must be added to the correction value. Therefore,

$$\eta^{\text{OER}} = \frac{\max\{\Delta G_1, \, \Delta G_2, \, \Delta G_3, \, \Delta G_4\}}{e} - 1.23 \tag{16}$$

2.3. Ir-Based Substrates and Selected Intermediates.

We selected well-defined Ir-based substrates, which includes Ir-metals and diversely composed oxides, 36,37 with the aim to improve our atomistic understanding of the evolution reactions of hydrogen and oxygen. 38,39 A top and side views of the Ir(100), Ir(111), IrO₂(110), IrO₂(100), α -Ir₂O₃(0001), and α -Ir₂O₃(1010) surfaces are depicted in Figure 3 along with the most important adsorption sites. The repeated slab geometries are composed of 5 Ir layers, respectively, while a vacuum

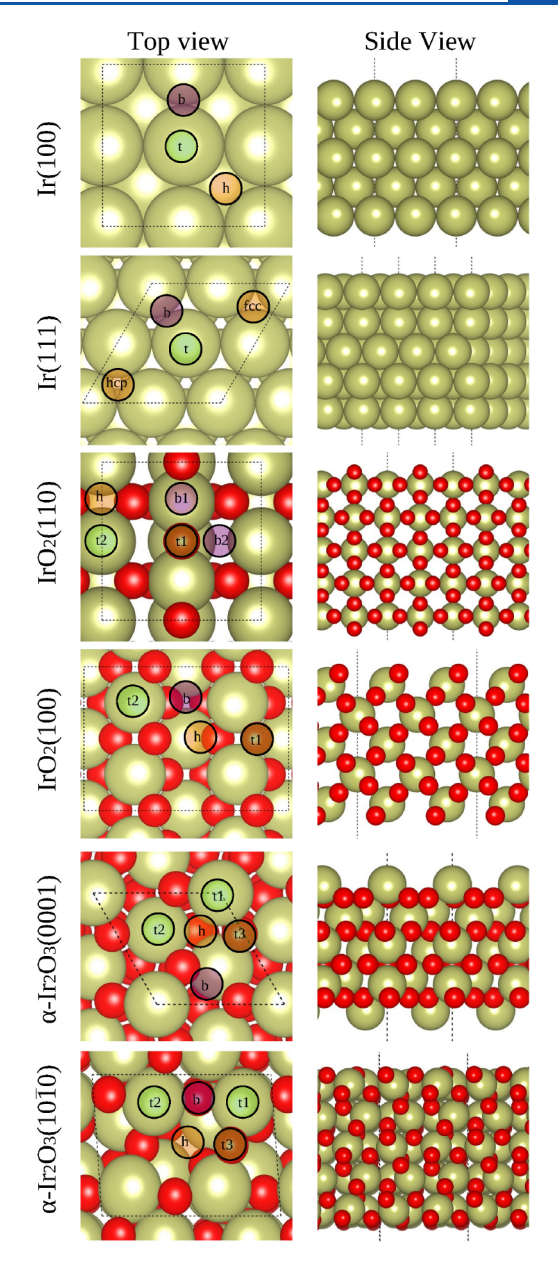


Figure 3. Top and side views of the slabs for iridium-based materials, with the adsorption sites highlighted. In the simplified nomenclature, the sites are classified as top (t), bridge (b), and hollow (h). Red spheres represent oxygen atoms, while dark yellow spheres correspond to iridium atoms.

spacing of 15 Å separates the slabs from its images, which yields negligible interactions among the slabs.

The adsorption sites exposed to the vacuum region on these surfaces are classified as top (t), bridge (b), and hollow (h) sites, with the latter further distinguished into face-centered cubic (fcc) and hexagonal closed-packet (hcp) varieties for densely packed surfaces such as Ir(111). Correct exploration of the adsorption sites plays an important role in the characterization of the adsorption properties because they directly affect the electronic interactions between the adsorbate and surface and hence determine the adsorption strength and catalytic activity. To take advantage of the symmetry, the adsorbates were placed on both sides of the slab, and hence, dipole corrections were not considered for the present calculations.

During this process, the atoms in the center of the slab are frozen in their bulk-like positions.

The selection of the facets was guided by the reported thermodynamic stability of metallic Ir, IrO₂, and α -Ir₂O₃ in the literature, with a secondary facet chosen for its perpendicular orientation relative to the most stable facet, thereby enabling the exploration of distinct coordination environments. Ir(111) is widely recognized as the most stable surface among the fcc Ir slabs, exhibiting lower surface energies compared to Ir(100) and Ir(110) surfaces. For IrO₂, previous computational studies indicate that the (110) plane represents the thermodynamically favored surface, as it minimizes the number of broken bonds per unit area, enhancing structural stability. Experimental investigations further reveal that the naturally forming layer of α -Ir₂O₃ aligns along the (0001) orientation of the corundum structure, with multilayer growth occurring via a Stranski–Krastanov mode. ⁴²

Metallic iridium surfaces, such as Ir(100) with its square-like configuration and Ir(111) with its hexagonal close-packed arrangement, are expected to present distinct reactivity profiles relative to iridium oxides (IrO_x) due to the presence of O species exposed to the vacuum region. Inclusion of Ir oxides, notably the (110) and (100) facets, which are recognized for their conductive behavior, along with the α -Ir₂O₃(0001) and (1010) facets, known for their semiconducting behavior. The selected facets are not restricted to the most stable forms for bulk metals (Ir(111)) and oxides (IrO₂(110)), but also embrace less conventional orientations to explore a wider range of coordination environments and surface terminations. For example, the α -Ir₂O₃(0001) facet, similar to the stable α - $Al_2O_3(0001)$ surface, and the perpendicular (1010) facet offer insight into how distinct crystallographic cuts reveal unique surface atom arrangements, thereby yielding varying catalytic potentials.

An improved understanding of hydrogen and oxygen evolution reactions necessitates a substantial number of calculations across a diverse array of species. However, utilizing the CHE model significantly reduces the number of DFT calculations. Geometric optimization was performed for all slabs. For the optimization of slabs with adsorbed species, the intermediate was initially placed on adsorption sites above and below the slab. The slab atoms were kept fixed, except for the two outermost layers. For each slab and adsorbed molecule, the most stable configuration, corresponding to the lowest adsorption energy, was selected for subsequent vibrational frequency calculations.

For the HER analysis, adsorbed H was studied, while for OER, the intermediates selected were adsorbed OH, O, and OOH, as these entities represent the reaction stages. For the adsorbed structures of polyatomic species (OH and OOH), the oxygen atom was initially oriented toward the slab for geometric optimization. This starting configuration is justified by the well-established behavior related to high electronegativity, the presence of lone pairs, and covalent interaction. In addition, the gas phase H₂ and H₂O were calculated, as they represent the reactants and products of HER and OER, respectively.

2.4. Physical-Chemical Properties. 2.4.1. Geometric Parameters. The coordination number is a classical descriptor defined as the number of nearest neighbors of a given atom. To refine this concept, its used here is the effective coordination number (ECN), which incorporates distance-dependent weights to account for partial bond contributions. ^{44,45} The

average bond length around the atom i is computed self-consistently as

$$d_{\text{av}}^{i} = \frac{\sum_{j} d_{ij} \exp\left[1 - \left(\frac{d_{ij}}{d_{\text{av}}^{i}}\right)^{6}\right]}{\sum_{j} \exp\left[1 - \left(\frac{d_{ij}}{d_{\text{av}}^{i}}\right)^{6}\right]}$$

$$(17)$$

Thus, the effective coordination number is then calculated using

$$ECN^{i} = \sum_{j} exp \left[1 - \left(\frac{d_{ij}}{d_{av}^{i}} \right)^{6} \right]$$
(18)

This formulation ensures that atoms farther away contribute less to the coordination environment, providing a continuous and chemically meaningful measure of atomic connectivity.

2.4.2. Energetic Properties. 2.4.2.1. Cohesive Energy. The thermodynamic stability of each material system was initially evaluated by calculating the cohesive energy $(E_{\rm coh})$, defined as

$$E_{\rm coh} = \frac{E_{\rm tot}^{\rm bulk} - \sum_{i} n_{i} E_{\rm tot}^{\rm free-atomi}}{\sum_{i} n_{i}}$$
(19)

where $E^{\rm bulk}$ denotes the total energy of the relaxed bulk unit cell, $E_i^{\rm free-atom}$ corresponds to the total energy of the isolated atom of type i calculated under consistent settings used for gasphase species, and n_i represents the number of atoms of element i in the unit cell. This metric provides a fundamental measure of the internal cohesion of the solid and allows for a relative comparison of the structural stability across different materials.

2.4.2.2. Formation Energy. To further assess the thermodynamic viability of oxide formation, the energy of formation per atom $(\Delta E_{\rm f}^{{\rm Ir}_n{\rm O}_n})$ for a generic iridium oxide compounds ${\rm Ir}_m{\rm O}_n$ was calculated using the expression,

$$\Delta E_{\rm f}^{{\rm Ir}_m{\rm O}_n} = \frac{E_{\rm tot}^{{\rm Ir}_m{\rm O}_n} - mE_{\rm tot}^{{\rm Irbulk}} - \frac{n}{2}E_{\rm tot}^{{\rm O}_2}}{m+n} \tag{20}$$

where $E_{\rm tot}^{\rm Ir_mO_n}$ is the total DFT energy of the oxide unit cell (IrO₂ or α –Ir₂O₃, in our case), $E_{\rm tot}^{\rm Ir \ bulk}$ is the cohesive energy per atom of the bulk iridium and $E_{\rm tot}^{\rm Lr}$ denotes the total energy of an oxygen molecule in the gas phase. These energetic descriptors are essential for comparing the thermodynamic stability of various compositions and crystal structures. By combining cohesive energy and formation energy analyses, one can identify the most stable compositions and gain insights into compound formation.

2.4.2.3. Surface Energy. To quantify the energetic cost associated with creating a slab from its corresponding bulk reference material, the surface energy (σ) is defined as

$$\sigma = \frac{E_{\text{tot}}^{\text{slab}} - N_{\text{bulk}} E_{\text{tot}}^{\text{bulk}}}{2A} \tag{21}$$

where $E_{\rm tot}^{\rm slab}$ denotes the total energy of the fully relaxed slab supercell, $E_{\rm tot}^{\rm bulk}$ is the energy per atom in the bulk reference system, $N_{\rm bulk}$ represents the number of slab atoms equivalent to those in the bluk, and A is the surface area of a single face of the slab. The factor of 2 in the denominator accounts for the two equivalent surfaces present in the symmetric slab model used in the calculations. This formulation is critical within the slab approach, as it inherently assumes that only the outermost

atomic layers are susceptible to significant relaxation and modification of properties, while the central region of the slab retains a bulk-like character, preserving the intrinsic features of the parent crystal structure.

2.4.2.4. Gibbs Free Energy. The strength of the interaction between the adsorbates and the substrate can be quantitatively evaluated through the adsorption energy ($\Delta E_{\rm ad}$) and the Gibbs free energy of the adsorption ($\Delta G_{\rm ad}$), defined by the following equation,

$$\Delta E_{\rm ad} = E_{\rm tot}^{\rm mol/subs} - E_{\rm tot}^{\rm mol} - E_{\rm tot}^{\rm subs}$$
 (22)

and

$$\Delta G_{\rm ad} = G_{\rm tot}^{\rm mol/subs} - G_{\rm tot}^{\rm mol} - E_{\rm tot}^{\rm subs}$$
 (23)

respectively. Here, $E_{\rm tot}^{\rm mol/subs}$ and $G_{\rm tot}^{\rm mol/subs}$ denote the total electronic energy and the Gibbs free energy of the adsorbate—substrate system, respectively. $E_{\rm tot}^{\rm subs}$ corresponds to the total energy of the clean slab substrate, while $E_{\rm tot}^{\rm mol}$ and $G_{\rm tot}^{\rm mol}$ refer to the total and free energies of the isolated molecule in the gas phase.

For the H* intermediate, the reference energy and the free energy are taken as $\frac{1}{2}E^{H_2}$ and $\frac{1}{2}G^{H_2}$, respectively. In contrast, direct use of molecular O2 as a reference for O* is avoided due to the known inaccuracies associated with its DFT-based description. Instead, the oxygen reference is approximated via the water formation reaction, using $E^{H_2O} - E^{H_2}$ and $G^{H_2O} - G^{H_2}$ to estimate the thermodynamic quantities of atomic oxygen. With respect to the substrate, thermodynamic corrections to the free energy of the clean surface are omitted, justified by the negligible structural rearrangements induced by the adsorption process.⁴⁶ This assumption is supported by the minimal geometric distortion observed in the surface atoms upon binding to adsorbate, as confirmed by the detailed test analysis provided in the electronic Supporting Information. Therefore, the rigid-slab approximation is considered valid, introducing only marginal errors in the thermodynamic quantities of the adsorbed species.

Corrections applied to ΔG convert these values for each PCET step by accounting for the U as well as the proton activity, expressed through the media's pH, relative to the standart Hydrogen Electrode (SHE) reference, according to the equation:

$$\Delta G(U) = \Delta G - eU - k_{\rm B} T \ln(10) \cdot pH \tag{24}$$

These adjustments ensure that the computed free energies accurately reflect the electrochemical environment and enable a direct comparison of reaction energetics under media conditions. The condition in which U satisfies $\Delta G(U)=0$ defines the permissible combinations of potential U and pH, thereby enabling the construction of the Pourbaix diagram.

2.4.3. Electronic Properties. 2.4.3.1. Work Function. The work function (Φ) represents a fundamental electronic characteristic that significantly influences the regulation of electron transfer phenomena. Φ is defined by the following equation,

$$\Phi = V_{\rm es}(\mathbf{r}_{\rm vac}) - E_{\rm Fermi} \tag{25}$$

where $V_{\rm es}({\bf r}_{\rm vac})$ represents the planar averaged electrostatic potential at a point in the vacuum region sufficiently far from the surface, and $E_{\rm Fermi}$ denotes the Fermi level of the slab system.

2.4.3.2. Effective Bader Charges. To further improve our understanding of charge redistribution induced by adsorption, Bader charge analysis was used. This method partitions the total charge density into atomic regions delineated by zero-flux surfaces of the charge density gradient field. The effective Bader charge on the atom i is computed as

$$Q_{\text{eff}}^{i} = Z_{\text{val}} - Q_{\text{Bader}}^{i} \tag{26}$$

where $Q_{\rm Bader}^i$ is the total number of electrons assigned to atom i through Bader partitioning, and $Z_{\rm val}$ is the number of valence electrons. A negative value of $Q_{\rm eff}^i$ indicates electron accumulation, whereas a positive value reflects electron depletion. Although Bader charges do not directly correspond to formal oxidation states, they can be used as a robust descriptor to evaluate local charge transfer among chemical species. ⁴⁸

3. RESULTS AND DISCUSSION

In this study, conducted step by step, the presentation and discussion of our findings have been systematically structured as follows. This analysis encompasses the properties of bulk and slab structures, followed by a discussion of adsorption and thermodynamic properties, concluding with a correlative analysis of these properties in relation to electrocatalytic performance.

3.1. Bulk Properties of Ir-Based Materials. Selected bulk properties are reported in Table 1. As anticipated,

Table 1. Bulk Properties of Ir-Based Compounds: Equilibrium Lattice Parameters $(a_0 \text{ and } c_0)$ Both in Å, Fundamental Electronic Band Gap $(E_{\rm g})$ in eV, d-Band Centers in eV, Average Distance $(d_{\rm av})$ in Å, Effective Ionic Radius $(r_{\rm eff}^{\rm Ir})$ in Å, Average Effective Coordination Number (ECN $_{\rm av}$) in the Number of Nearest Neighbors (NNN), and Cohesive Energy Per Atom in eV

properties	Ir	IrO_2	α -Ir ₂ O ₃
a_0	3.83	4.51	5.25
c_0		3.17	13.25
$d_{ m av}^{ m Ir}$	2.71	1.99	2.08
$r_{ m eff}^{ m Ir}$		0.60	0.68
$d_{\mathrm{av}}^{\mathrm{O}}$		2.00	2.09
$\mathrm{ECN}_{\mathrm{av}}^{\mathrm{Ir}}$	12.02	6.15	6.08
ECN_{av}^{O}		3.20	4.11
$E_{ m g}$	metal	metal	0.79
$\epsilon_{ m d}$	-3.19	-4.21	-3.21
$\epsilon_{ m p}$		-5.37	-6.02
$\Delta\epsilon$		1.16	2.81
E_{coh}	-8.06	-5.56	-2.54

oxidation of the bulk Ir in its oxidized forms with varying O compositions involves a significant transformation from metallic conductivity to semiconductive behavior and changes in the Ir oxidation state, accompanied by a noticeable decrease in the energetic stability of the bulk, as quantified by the cohesive energy per atom. Moreover, oxidation induces a decrease in volume per atom, as evidenced by the transformation from the metallic Ir bulk in the fcc structure (14.04 ų, Ir³) to the α -Ir₂O₃ trigonal corundum structure (11.09 ų, Ir³+), and later to the IrO₂ rutile structure (10.76 ų, Ir⁴+).

This trend is consistent with the reduction of the ionic radius of Ir as its oxidation state increases. According to Shannon, 49 the ionic radii of Ir 0 , Ir $^{3+}$, and Ir $^{4+}$ in octahedral

Table 2. Structural and Electronic Properties of the Atoms Most Exposed to Vacuum on Ir-Based Slabs^a

properties	Ir(111)	Ir(100)	IrO ₂ (110)	IrO ₂ (100)	α -Ir ₂ O ₃ (0001)	α -Ir ₂ O ₃ (10 $\overline{1}$ 0)
$\mathrm{ECN}_{\mathrm{av}}^{\mathrm{Ir}}$	9.01	8.05	5.24	5.10	3.30	4.69
ECN_{av}^{O}			2.28	2.34	3.11	2.52
Φ	5.50	5.55	6.02	6.09	4.88	5.92
Qeff, av	-0.06	-0.06	1.26	1.59	1.02	1.21
Q ^O _{eff, av}			-0.66	-0.87	-0.91	-0.82
ϵ_d	-3.02	-2.88	-3.83	-3.71	-3.12	-3.10
ϵ_p			-4.85	-4.70	-5.78	-5.16
$\Delta\epsilon$			1.02	0.99	2.66	2.06
$\sigma_{ m s}$	210	246	123	152	98	204

^aThe work function (φ), O p-band center, Ir d-band center, and their energy difference ($\Delta \epsilon$) are reported in eV. Average Effective Bader charges ($Q_{eff, av}^{Ir}$ and $Q_{eff, av}^{O}$) are given in units of ϵ , while the average effective coordination number (ECN) corresponds to the number of nearest neighbors (NNN). The surface energy (σ_s) is reported in meVÅ⁻².

coordination are 1.35, 0.68, and 0.625 Å, respectively. Additionally, effective ionic radii for Ir were estimated from the average Ir–O bond lengths $(d_{\rm av})$, using the relation $r_{\rm eff}^{\rm Ir}=d_{\rm av}^{\rm Ir}-1.40$, where the value of 1.40 Å for the ionic radius of ${\rm O}^{2-}$ in octahedral coordination is also taken from Shannon. This yields the values in Table 1, which are in good agreement with the values in the literature and reflect the impact of oxidation on the local atomic environment. It is important to note that the corundum and rutile structures are more open than the compact fcc lattice, and the coordination geometry may influence the effective radii. Finally, the calculated lattice parameters exhibit excellent agreement with the values from both the computational and experimental literature, with deviations not exceeding 1% for all bulk compounds. $^{41,50-53}$

As mentioned, the fundamental electronic band gap (E_g) shows a transition in electronic properties. For example, metallic in Ir and IrO2, for instance, manifest an absence of a band gap, thereby corroborating their conductive properties in agreement with empirical data on IrO₂. 41,54 Conversely, α -Ir₂O₃ is characterized by an indirect band gap of 0.79 eV, thus categorizing it as a semiconductor. As expected, the calculated band gap is observed to be lower than those derived from advanced experimental (approximately 3.00 eV)¹⁶ and accurate hybrid-HSE calculations (2.9 eV). 53 This discrepancy can be attributed to a well-known self-interaction error inherent in GGA functionals. For example, because of its inherently continuous and differentiable characteristics, the PBE functional often fails to accurately capture the discontinuous electronic behavior that is indicative of band gaps, leading to lower estimated values compared to empirical measurements.

The *d*-band centers (ϵ_d) and the *p*-band centers (ϵ_p) offer information on electronic interactions between iridium and oxygen. The Ir d-band center shifts to a more negative energy (-4.21 eV) in IrO_2 compared to metallic Ir (-3.19 eV), suggesting a stronger interaction (hybridization) between Ir dorbitals and O p-orbitals, leading to a more localized and stabilized d-electron character in the oxide. Interestingly, α - Ir_2O_3 exhibits a slightly less negative *d*-band center (-3.21 eV) than IrO2. Concurrently, the O p-band center becomes progressively more negative (lower energy) from IrO2 (-5.37 eV) to $\alpha\text{-Ir}_2\text{O}_3$ (-6.02 eV), indicating greater stabilization of oxygen p-orbitals in the latter due to differences in local bonding environments and formal oxidation states. The energy separation between the d- and p-band centers ($\Delta \epsilon$ $=\epsilon_{p}-\epsilon_{d}$) further elucidates these interactions. For example, a lower $\Delta \epsilon$ indicates closer alignment of these band energies, which promotes stronger orbital hybridization and increased

covalency between transition metal d orbitals and oxygen p orbitals. The observed increase in $\Delta \varepsilon$ from ${\rm IrO_2}$ (1.16 eV) to $\alpha\text{-Ir_2O_3}$ (2.81 eV) therefore suggests that ${\rm IrO_2}$ exhibits a more hybridized nature and greater covalency between Ir and O compared to $\alpha\text{-Ir_2O_3}$. In the context of heterostructure electrocatalysts, this stronger hybridization in ${\rm IrO_2}$ is often correlated with enhanced OER activity, implying that $\alpha\text{-Ir_2O_3}$ might be comparatively less catalytically active for such processes due to its more ionic character.

The ECN can be used as a quantitative metric to assess local atomic bonding environments. The average ECN $_{\rm av}^{\rm Ir}$ values exhibit a significant reduction from 12.02 NNN (metallic Ir bulk) to approximately 6 NNN for both the IrO $_{\rm 2}$ and $\alpha\text{-Ir}_{\rm 2}O_{\rm 3}$ oxides. Thus, each Ir atom is typically coordinated by six O atoms within an octahedral or a distorted octahedral arrangement. Although the ECN $^{\rm Ir}$ values for both oxides show similarities, the ECN for oxygen (ECN $^{\rm O}$) shows critical structural differences: it rises from IrO $_{\rm 2}$ (3.20 NNN) to α -Ir $_{\rm 2}O_{\rm 3}$ (4.11 NNN). This implies that oxygen atoms exhibit an increased number of coordination with Ir neighbors in α -Ir $_{\rm 2}O_{\rm 3}$, influencing their packing density and indicating a pronounced ionic character for α -Ir $_{\rm 2}O_{\rm 3}$. As suggested by Phillips' concept, ⁵⁵ the ECN $^{\rm O}$ values may reflect enhanced ionicity, which could affect the adsorption of chemical species in HER and OER.

Upon oxidation, iridium undergoes a notable change in stability. Although bulk metallic Ir possesses a cohesive energy of -8.06 eV, its oxide forms IrO_2 (-5.56 eV) and α - Ir_2O_3 (-2.54 eV), exhibit a considerably reduced magnitude of negative cohesive energy. This trend signifies a decrease in the energetic stability of the material when forming the oxides. This observation clearly suggests that metallic Ir exhibits the greatest bulk stability, followed by IrO_2 , whereas α - Ir_2O_3 is the least thermodynamically stable in its bulk form. Although the cohesive energy calculated for metallic Ir is overestimated by approximately 17% compared to the experimental values, ⁵⁶ i.e., possibly due to the attractive bias characteristic of D3 vdW correction, however, this systematic discrepancy does not hinder the comparative evaluation of material stability. The elevated cohesive energy of metallic Ir aligns with its more compact lattice structure and robust metallic bonding, while the lower cohesive energies observed for oxides are attributable to the predominant directional bonding, which is intrinsically less energetically favorable than the prominent delocalized bonding in metals.

Lastly, the formation energies offer further thermodynamic insight. The calculated values, $\Delta H_{\rm f}^{\rm IrO_2} = -0.793$ eV/atom and $\Delta H_{\rm f}^{\rm Ir_2O_3} = -0.278$ eV/atom, clearly indicate that the 4+

oxidation state of iridium in IrO_2 is thermodynamically more stable than the 3+ state in α - Ir_2O_3 . This is consistent with the stronger bonding and the higher coordination symmetry present in the rutile structure, which contribute to the favorable formation energy of IrO_2 .

3.2. Characterization of the Surface Properties of **Clean Surfaces.** Table 2 presents the energetic and electronic parameters for all slabs based on Ir. The values of the work function for Ir(111) and Ir(100) show slight deviations from the experimentally determined literature values of 5.76 and 5.67 eV,⁵⁷ respectively. In addition, they align with previously reported DFT+PBE calculated values of 5.50 and 5.55 eV from the literature.⁵⁸ For IrO₂(110), the work function deviates by less than 1% from previous values obtained using the same computational methodology. 59 ECN values indicate that pure metal slabs are more compact than oxides. In IrO2, iridium atoms exhibit higher coordination than in α -Ir₂O₃. In contrast, oxygen atoms in IrO2 have lower ECN values, suggesting greater exposure and consequently more favorable sites for reaction intermediate adsorption on that slab. Such properties for IrO₂(100), being a less stable cut, as well as for $Ir_2O_3(0001)$ and $Ir_2O_3(10\overline{10})$, are not extensively reported in the literature due to their derivation from the less explored version of the iridium oxidation state.

Analyzing Figure 4, a similar electronic property behavior is observed for both metallic iridium slabs. They feature a broader d-band spreading, characteristic of pure 5d metals. One explanation for assessing the catalytic propensity of a transition metal, within the classical Hammer–Nørskov model, stems from the direct relationship between the proximity of the center of the d band to the Fermi energy ($E_{\rm Fermi}$) and the adsorption energy. For this analysis, only the most exposed atoms of the first layer are considered for DOS contributions. The metallic Ir and IrO₂ slabs retain their metallic character, consistent with their bulk structures. Conversely, for α -Ir₂O₃, the (0001) cut exhibits a electronic band gap of 0.46 eV (smaller than the bulk), demonstrating semiconducting behavior, as observed in the corundum-like bulk

The $(10\overline{10})$ cut, however, shows metallic behavior without a band gap. A decrease in the band gap for semiconductor slabs compared to their bulk counterparts is expected. This occurs because the more exposed oxygen atoms lose coordination, which directly influences the interaction of their p orbitals, leading to increased dispersion of electronic states, compounded by the GGA's inherent band gap underestimation. The lower coordination of oxygen drastically alters the band gap, potentially changing the material's behavior from semiconducting to metallic. This observation correlates with the higher ECN^O of the (0001) cut compared to the $(10\overline{10})$ cut. A similar phenomenon occurs with α -Fe₂O₃(0001), slab in which metallization occurs.

The thermodynamic stability of the slabs is characterized by the surface energy σ_s , through which it is evident that all investigated systems, including metallic Ir, rutile and corundum-like structures, exhibit trends consistent with previous literature. Specifically, Ir(111), IrO₂(110), and Ir₂O₃(0001) emerge as the most stable facets for their respective bulk phases, which confirms previous computational findings. The slabs Ir(111) and Ir(100) also display elevated values of the average effective coordination number (ECN_{av}), consistent with their higher surface stability. In particular, among the corundum-like configurations,

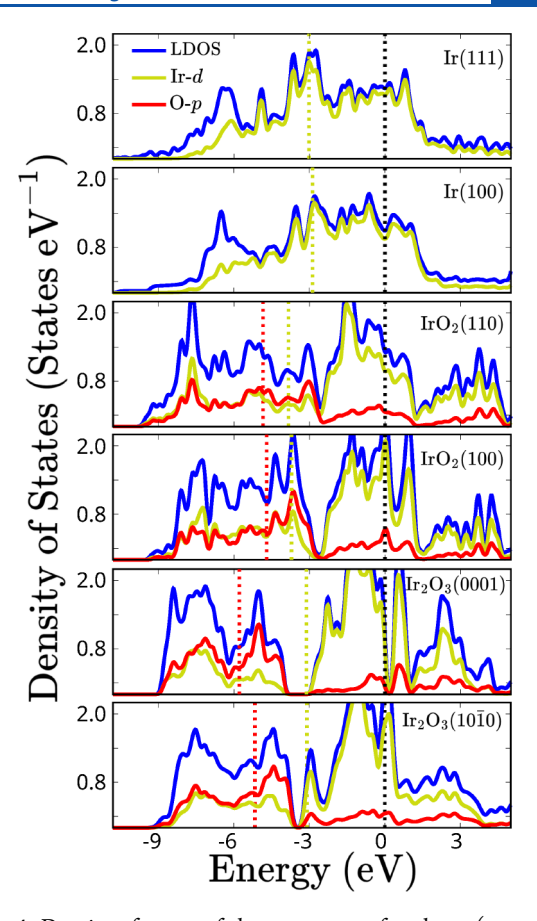


Figure 4. Density of states of the topmost surface layer (exposed to the vacuum region): Sum of the local density of states contributions (LDOS, in blue) and Ir *d*-states (dark yellow) and O *p*-states (red) contributions, normalized per atom. The zero energy, indicated by black dashed vertical lines, is referenced to either the Fermi level (for metallic systems) or to the valence band maximum (for semi-conductors). The calculated *d*- and *p*-band centers are shown as dashed lines matching the color of the corresponding LDOS.

 $\rm Ir_2O_3(0001)$ is the most stable facet, despite its iridium atoms being less coordinated relative to those of metallic and rutile-like slabs. This observation underscores a broader trend in which materials with higher local coordination density tend to exhibit higher surface energy, a relationship that aligns well with established theoretical predictions and previous studies.⁶⁵

Figure 5 presents the relative average effective Bader charge (ΔQ^{lr}) , calculated as the deviation from the highest reference value for each of the three distinguishable layers within the five-layer slab: the top surface layer, the subsurface layer and the central bulk-like region. Due to the inherent symmetry of the slab model, only these three layers exhibit unique charge environments. This analysis elucidates the spatial variation in the electronic charge distribution along the slab depth and highlights the magnitude of the electronic perturbation induced by the effects of surface termination. In addition to exhibiting the highest average effective coordination number (ECN_{av}), as previously discussed, iridium atoms located in the top surface layer of the metallic slabs show a nearly neutral charge distribution, with $Q_{\rm eff, av}^{\rm Ir} \approx -0.06$ e. This minimal deviation between the bulk-like and surface layers indicates a highly homogeneous electronic environment across the slab, suggesting negligible internal polarization. This electronic

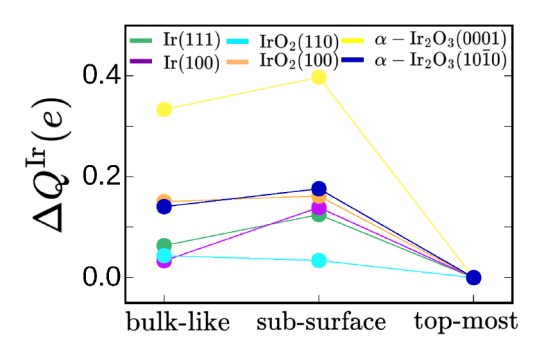


Figure 5. Average effective Bader charge for Ir atoms, computed relatively to the reference value $Q_{\rm eff,\ av}^{\rm Ir}$ (Table 2) of the topmost surface layer, evaluated for the three outermost atomic layers of the five-layered clean slabs.

uniformity correlates with higher σ_{s} , as less surface-induced relaxation occurs.

In contrast, the α -Ir₂O₃(0001) surface exhibits the lowest surface energy among all systems studied and is characterized by pronounced internal polarization. This is evidenced by significantly more positive effective Bader charges in both the bulk-like and subsurface layers compared to the topmost layer. Such a charge redistribution implies substantial internal stabilization, where the outermost layer is notably less oxidized than the interior of the slab. As a consequence, the outermost atomic layer is expected to display surface chemical properties more similar to those of metallic iridium. This inference is further supported by the observation that, among all oxide terminations, the lowest Q_{eff, av} is found for iridium atoms in the top layer of the α -Ir₂O₃(0001) slab. The thermodynamic stability of the $Ir_2O_3(10\overline{10})$ surface is comparable to that of the oxidized iridium phases, namely the IrO2 slabs. Moreover, the electronic properties reveal that these three slabs exhibit highly similar charge distributions, particularly with respect to the effective Bader charge of surface iridium atoms. The Qeff. av values for the top layers are nearly equivalent across these oxides, indicating analogous electronic surfaces and a consistent degree of iridium oxidation at the vacuum interface.

3.3. Lowest Energy Adsorbed Structures. Figure 6 presents the adsorption configurations corresponding to the most stable adsorption sites for each investigated slab. These specific configurations, identified as those that exhibit the lowest adsorption energies, were employed in subsequent thermodynamic analyzes and electrochemical evaluations. The selection criterion for each adsorbate—slab combination was strictly based on energetic stability, ensuring that only the most thermodynamically favorable adsorption geometries were considered.

Hydrogen adsorption on metallic surfaces has been extensively studied across a wide range of materials, allowing for direct comparison of adsorption preferences. In the case of hydrogen on Ir(111), adsorption is favored at the top site, whereas on Ir(100), the bridge site is energetically preferred. These findings are consistent with previous reports in the literature. 66,67 Platinum, which has been extensively investigated with respect to the adsorption of atomic hydrogen,⁶⁸ exhibits structural similarity to iridium due to its FCC lattice. However, a different behavior emerges in the context of adsorption on the (111) surface. In Pt(111), hydrogen atoms preferentially bind to hollow sites, 69 a preference attributed to the higher filling of the d orbitals in platinum compared to iridium. This increased d-band occupancy leads to a modification in the electronic environment at the surface, rendering the top site energetically less favorable for adsorption. Consequently, the electronic structure of Pt promotes a stronger interaction of hydrogen with hollow sites, compared to Ir(111), where the top site may become more accessible due to the comparatively lower filling of the dorbitals in iridium.

It is well established that intermediates tend to preferentially adsorb on the bridge sites of Ir(100). In contrast to structurally similar Ir(111), which features 3-fold hollow sites, Ir(100) has 4-fold coordinated sites. This difference significantly influences the interaction between the adsorbates and the surface, as they preferentially bind to the sites with higher coordination, where the electronic density of the transition metal is more

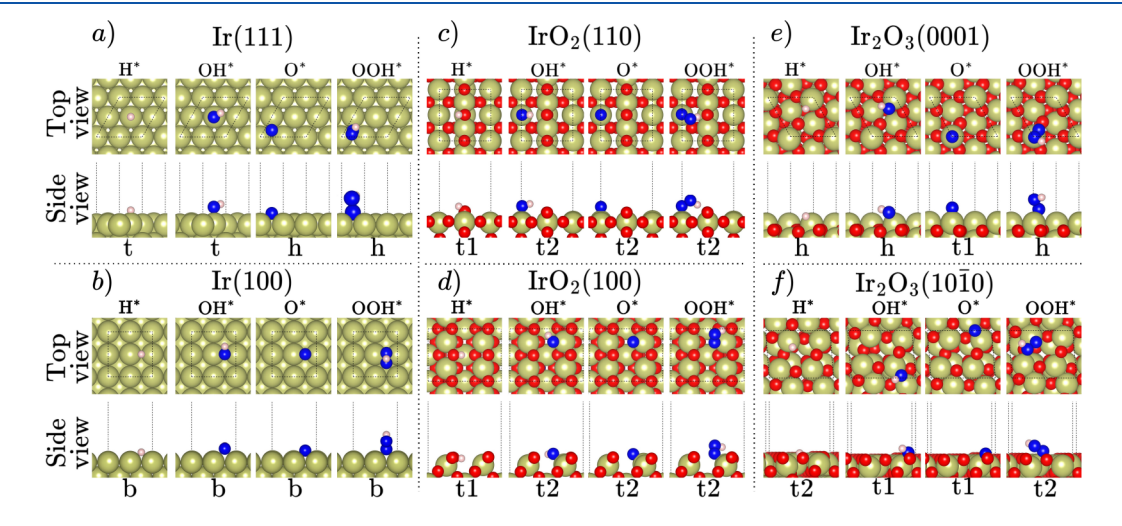


Figure 6. Top and side views of the optimized adsorption configurations of reaction intermediates (H*, OH*, O*, and OOH*) on different iridium-based surfaces relevant to HER and OER. Each column corresponds to a specific intermediate, and each row to a distinct surface: (a) Ir(111), (b) Ir(100), (c) $IrO_2(110)$, (d) $IrO_2(100)$, (e) $Ir_2O_3(0001)$, and (f) $Ir_2O_3(1010)$. Atoms in light pink, blue, red, and dark yellow represent hydrogen, oxygen from the adsorbed species, oxygen from the slab, and iridium, respectively. The labels (t, h, and b) denote top, hollow, and bridge adsorption sites.

ı

delocalized between the four atoms due to the orientation of the metal orbitals. 70

Notably, on oxide substrates, adsorption preferentially occurs at top sites, where a direct bond is established between the reaction intermediates and a single surface atom. This preference arises from the low coordination environment of surface atoms in the oxide lattice, which limits the spatial proximity required for effective orbital overlap between the intermediates and neighboring iridium or oxygen atoms at multifold sites. As a result, the formation of bonds at hollow or bridge sites becomes electronically unfavorable as a result of insufficient orbital interaction, making top-site adsorption energetically preferred in these systems.

In IrO₂ slabs, hydrogen preferentially adsorbs at top sites coordinated with surface oxygen atoms, while other intermediates, whose terminal atoms are oxygen, tend to adsorb atop iridium atoms. This behavior can be attributed to the difference in electronegativity between the adsorbates and the surface atoms: oxygen-terminated intermediates interact more favorably with iridium sites, allowing for a stronger chemical bond as a result of enhanced charge polarization. In all these adsorption configurations, the surface atoms involved exhibit lower coordination numbers, as highlighted in Table 2, which further favors adsorption by increasing the interaction of these undercoordinated sites.

In contrast, on the $\rm Ir_2O_3$ surfaces, all adsorbed intermediates are consistently anchored at sites in close proximity to iridium atoms. This behavior can be rationalized by the structural characteristics of the (0001) termination, where surface iridium atoms are more exposed to the vacuum region, while the oxygen atoms are predominantly subsurface. Even in hollow adsorption sites, the terminal adsorbates are located closer to iridium atoms than to oxygen atoms because of the surface topology. On the $\rm Ir_2O_3(1010)$ facet, adsorption occurs exclusively on top of the iridium atoms, with variations arising only from the specific iridium sites involved in the interaction. These distinct adsorption motifs reflect the anisotropic nature of the exposed surfaces and the distribution of iridium coordination environments, which directly influence the adsorption geometry and binding characteristics of reaction intermediates.

The proximity of hydrogen atoms to surface oxygen atoms upon adsorption on IrO_2 slabs reveals a significant difference in the nature of the slab—adsorbate interaction, as illustrated in Figure 7. In these cases, hydrogen undergoes a pronounced charge redistribution due to its interaction with surface oxygen, resulting in a relatively positive effective Bader charge $(Q_{\rm eff}^{\rm H})$.

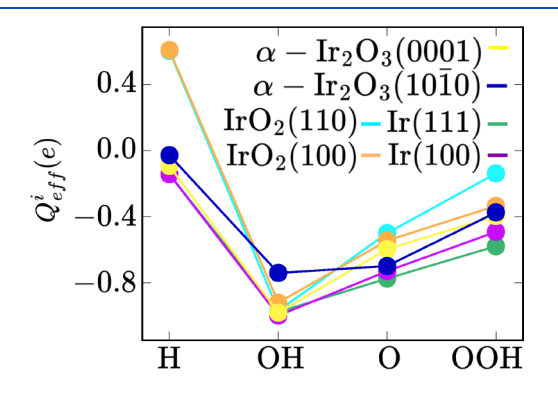


Figure 7. Effective Bader charge on the terminal atom *i* within the intermediates H, OH, O, and OOH adsorbed on Ir-based substrates.

This contrasts with adsorption on other slabs, where the hydrogen atom is more closely associated with surface iridium atoms rather than oxygen, and the resulting charge transfer is more moderate because of the smaller electronegativity difference between hydrogen and iridium.

For oxygenated intermediates, the terminal atoms that interact with the surface are invariably oxygen, and the corresponding effective Bader charges (Qeff), evaluated for the oxygen atom closest to the slab, are consistently negative upon adsorption, as expected. Due to the more uniform charge distribution on the metallic slabs, as reported in Table 2, charge donation from the surface to the adsorbed oxygencontaining species is more efficient on the metallic substrates. In contrast, on oxide slabs where surface oxygen atoms are more readily accessible, there is a tendency for the slab to retain a greater portion of the electronic charge, thereby limiting charge transfer to the adsorbed oxygen atoms. This behavior becomes increasingly evident for the intermediates O and OOH, where the molecular oxygen atoms exhibit lower Q_{eff}^{O} values on the IrO₂ slabs compared to those on metallic Ir, which facilitates more substantial charge transfer. The corundum-like slabs display an intermediate response, attributable to their more coordinated (and thus less exposed) surface oxygen atoms, which modulate the charge-exchange dynamics with the adsorbates.

The analysis presented in Figure 8 is crucial for elucidating the electronic factors that govern adsorption strength. Subtle

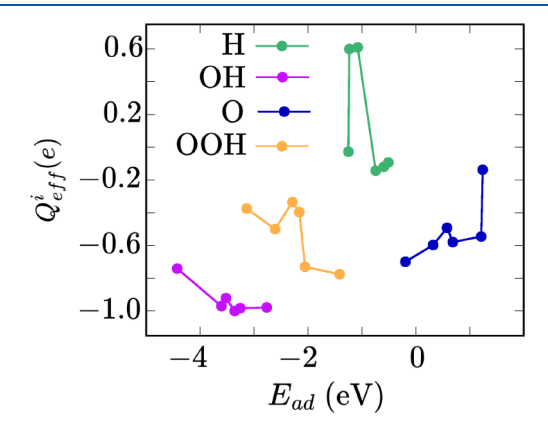


Figure 8. Correlation analysis of the effective Bader charge of the terminal atom i in the intermediates H, OH, O, and OOH with their corresponding adsorption energies on the substrates.

variations in the effective Bader charge of the terminal atom, the atom of the molecule closest to the substrate, correlate with substantial changes in $E_{\rm ad}$, thereby modulating the catalytic activity. Examining the green curve, it becomes evident that H* exchanges only a minimal amount of charge with the surface (with effective charges close to zero), leading to adsorption energies clustered near zero. However, a few data points exhibit more positive effective charges, corresponding to stronger adsorption interactions, particularly when H donates charge to the IrO₂ substrates. For atomic O adsorption, a clear trend emerges in which more negative effective charges on the terminal oxygen correlate with increasingly negative adsorption energies. This observation is consistent with the expected electrostatic attraction between the anionic adsorbate and the positively polarized substrate sites, reaffirming the direct relationship between charge localization and binding strength.

Table 3. Adsorption Energy and Gibbs Free Adsorption Energy, Along with the Differential Contributions $\Delta(\text{ZPE})$, $\Delta(\int C_n dT)$, and $\Delta(-\text{TS})$ in eV^a

properties	Ir(111)	Ir(100)	IrO ₂ (110)	IrO ₂ (100)	α -Ir ₂ O ₃ (0001)	α -Ir ₂ O ₃ (10 $\overline{1}$ 0)
$E_{ m ad}^{ m H}$	-0.60	-0.75	-1.23	-1.08	-0.54	-1.25
$\Delta(\mathrm{ZPE})^{\mathrm{H}}$	0.06	0.04	0.18	0.18	0.09	0.09
$\Delta (\int C_p dT)^{\mathrm{H}}$	-0.03	-0.04	-0.04	-0.04	-0.04	-0.04
$\Delta(-TS)^{H}$	0.18	0.19	0.19	0.19	0.20	0.19
$\Delta G_{ m ad}^{ m H}$	-0.39	-0.56	-0.90	-0.75	-0.30	-1.00
$E_{ m ad}^{ m OH}$	-2.77	-3.36	-3.61	-3.52	-3.26	-4.43
$\Delta(\mathrm{ZPE})^{\mathrm{OH}}$	0.11	0.15	0.14	0.14	0.13	0.17
$\Delta (\int C_p dT)^{ m OH}$	0.02	0.00	0.00	0.00	0.01	-0.01
$\Delta(-TS)^{OH}$	0.38	0.45	0.43	0.43	0.41	0.46
$\Delta G_{ m ad}^{ m OH}$	-2.31	-2.82	-3.08	-2.97	-2.75	-3.85
$E_{ m ad}^{ m O}$	0.69	0.58	1.24	1.21	0.32	-0.19
$\Delta(\mathrm{ZPE})^{\mathrm{O}}$	-0.08	-0.08	-0.07	-0.07	-0.07	-0.07
$\Delta(\int C_p dT)^{\rm O}$	0.02	0.03	0.03	0.03	0.03	0.02
$\Delta(-TS)^{O}$	0.05	0.03	0.04	0.04	0.02	0.05
$\Delta G_{ m ad}^{ m O}$	0.62	0.49	1.16	1.14	0.24	-0.25
$E_{ m ad}^{ m OOH}$	-1.41	-2.06	-2.61	-2.29	-2.16	-3.14
$\Delta(\mathrm{ZPE})^{\mathrm{OOH}}$	0.06	0.03	0.07	0.09	0.07	0.08
$\Delta (\int C_p dT)^{OOH}$	0.04	0.05	0.02	0.02	0.04	0.03
$\Delta(-TS)^{OOH}$	0.15	0.13	0.21	0.20	0.15	0.18
$\Delta G_{ m ad}^{ m OOH}$	-1.14	-1.55	-2.01	-1.68	-1.60	-2.55

^aThese values represent the differences between the adsorbed intermediate configurations and the corresponding gas-phase intermediates for H, OH, O, and OOH.

Furthermore, a consistent pattern is observed for the terminal oxygen atoms in OH and OOH, where less negative Bader charges are associated with stronger adsorption. This behavior highlights an optimized charge-transfer regime in which the oxygen atoms of these species interact effectively with the substrate without inducing excessive electron depletion, particularly on oxidized surfaces, thus maintaining an optimal balance between surface stability and adsorbate interaction. Such fine-tuned charge redistribution reflects the delicate equilibrium that underpins efficient electrocatalysis, revealing how the interplay between oxidation state and charge transfer dictates the overall catalytic response.

3.4. The Role of the Thermodynamic Contributions to the Energetic Adsorption Properties. The raw DFT energy only accounts for the internal energy of the system and therefore provides an incomplete description of the adsorption process. In contrast, the Gibbs free energy incorporates translational, rotational, and vibrational contributions for gasphase molecules. Upon adsorption, the translational and rotational degrees of freedom are hindered, while the vibrational modes become restricted. Including these effects helps overcome the overbinding problem commonly associated with ΔE_{ad} , which can significantly affect the precision of catalytic performance analyzes.

Table 3 presents the adsorption energies along with the variations due to ZPE (as defined in eq 4), constant-pressure heat capacity (eq 5), and entropic (eq 6) corrections, which differentiate the thermodynamic values from the raw DFT energies. For H*, OH*, and OOH*, these corrections exert a significant impact on adsorption free energy, effectively attenuating the magnitude of $\Delta G_{\rm ad}$. The magnitude and complexity of these effects increase with the number of vibrational degrees of freedom and are particularly influenced by the substantial gas phase entropy, as observed in the case of OOH*. The entropic contribution associated with O* is lower compared to hydrogen-containing intermediates. This is

attributed to the inherently low entropy of both the reference species of the gas phase (H_2O) and H_2 and the adsorbed configuration. As a result, the overall entropic correction remains minimal in this case.

In none of the investigated cases do these corrections alter the relative stability ordering among the adsorbed configurations. Among all contributions, the entropic term is the most influential. This dominance arises from the hindrance of translational and rotational degrees of freedom upon adsorption, which significantly reduces the entropy of the molecule and thus plays a crucial role in achieving chemical accuracy. In contrast, although ZPE and the enthalpic terms may contribute appreciable absolute values, they exhibit minimal variation between the gas-phase and adsorbed states, as they primarily depend on vibrational properties.⁷¹

3.5. Hydrogen Evolution Reactions. Figure 9 displays the volcano plot curve constructed according to the CHE model, with the corresponding values provided in the Electronic Supporting Information. For comparison with similar PBE-based results, the value of $\Delta G_{\rm H^*}$ obtained here for Ir(111) is -0.39 eV, while the reference study reported

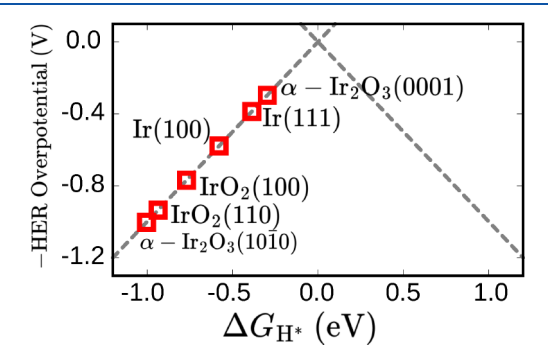


Figure 9. Volcano plot for HER with the gray dashed line serving as a reference based on the modular equation.

ACS Applied Energy Materials

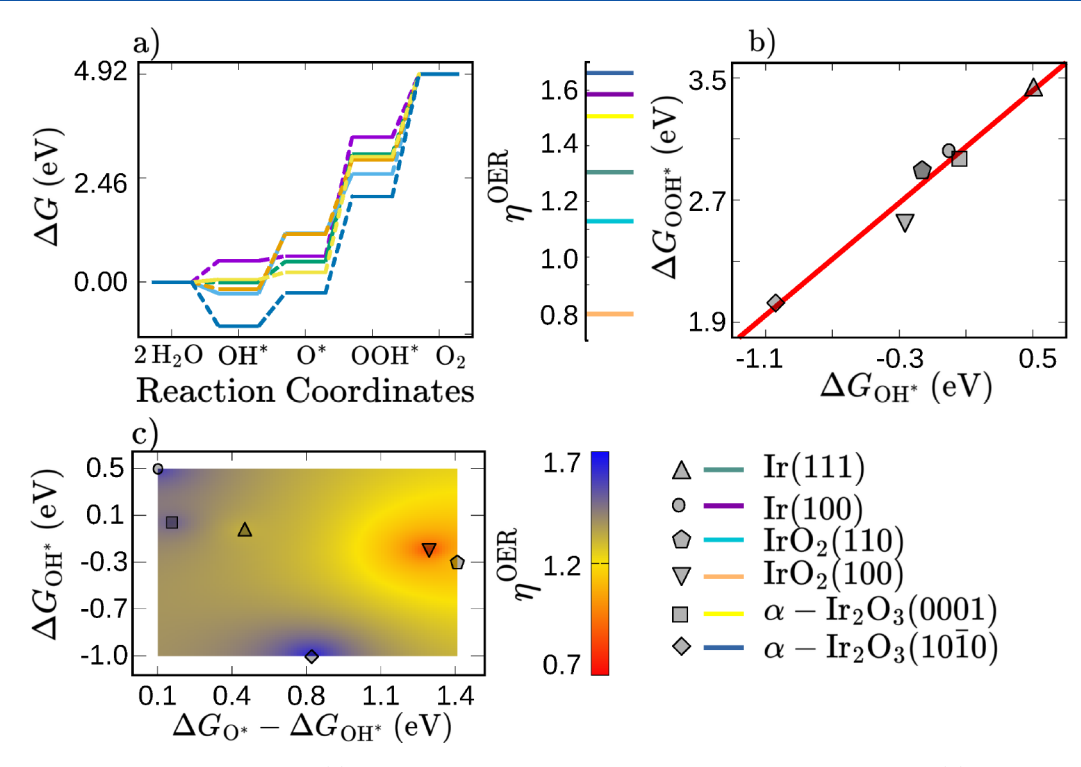


Figure 10. Performance of the slabs for OER. (a) Gibbs free-energy diagram and corresponding overpotentials. (b) Linear scaling relationship between the reaction states ΔG_{OOH^*} and ΔG_{OH^*} . (c) Two-dimensional volcano plot with color interpolation scales for the overpotential.

-0.37 eV, 72 representing a deviation of less than 5%. In particular, the data points align precisely with the gray dashed lines that shape the volcano curve, as the relationship between the free energy ΔG_{H^*} and the overpotential is analytical, as expressed in eq 10. All configurations indicate that the HER proceeds via the desorption step as the PDS, consistent with a strong adsorption regime, since the points lie on the left side of the volcano.

As predicted, Ir(111) and Ir(100) exhibit similar performance, consistent with their nature as surfaces composed of highly coordinated atoms, which leads to a reduced density of available electronic states. The weak interaction arises from the limited charge transfer between hydrogen and the substrate, which positions both surfaces very close to the top of the volcano curve. The IrO₂ slabs show comparable behavior among themselves, which can be attributed to similar coordination environments involving iridium and oxygen atoms on the various surfaces. This structural similarity leads to consistent electronic characteristics, as reflected in the values $\Delta \epsilon$, which do not indicate any significant changes in the degree of orbital mixing between the Ir and O atoms.

In contrast, when hydrogen is adsorbed on metallic iridium slabs, it exhibits a markedly different behavior. A particularly remarkable aspect arises in the case of hydrogen adsorption on $\alpha\text{-Ir}_2O_3$ surfaces. Among the terminations analyzed, the (0001) facet emerges as the most catalytically favorable, while the (1010) surface exhibits the least desirable performance due to the excessively strong binding of the reaction intermediate, which likely hinders the thermodynamics of the reaction. This discrepancy in the catalytic behavior can be traced back to differences in their electronic properties. Specifically, the outermost layers of the $\alpha\text{-Ir}_2O_3(1010)$ slab display a metallic-like character, in contrast to the semiconducting nature of the bulk phase, thereby modifying the surface's interaction with adsorbates. Additionally, the $\alpha\text{-Ir}_2O_3(0001)$

surface presents a relatively large $\Delta\epsilon$, suggesting limited orbital hybridization and, consequently, reduced ability to effectively adsorb and interact with reaction intermediates.

As discussed previously, the iridium atom most exposed to vacuum, responsible for binding all intermediates, exhibits a lower effective charge compared to subsurface layers and a lower average charge relative to other oxide slabs. This depletion of charge at the surface contributes to improved surface stability. Notably, this slab displays ΔG_{H^*} values comparable to those of metallic iridium surfaces. In contrast, α -Ir₂O₃(1010) is markedly less stable, exhibiting strong overbinding with intermediates and electronic characteristics more aligned with rutile-like oxides. These include similar instability, charge distribution profiles along the depth of the slab, and a comparable $\Delta \epsilon$, as previously highlighted. Consequently, HER performance across the different slab classes can be rationalized based on these electronic descriptors, which effectively differentiate the catalytic behavior of structurally distinct terminations, even when derived from the same parent material.

3.6. Oxygen Evolution Reaction. In this section, we systematically investigated the catalytic performance of six iridium-based surfaces toward the oxygen evolution reaction (OER). The Gibbs free energies of the key oxygen-containing adsorbates (ΔG_{OH^*} , ΔG_{O^*} , and ΔG_{OOH^*}) were calculated according to eq 3, taking the initial reference state as a clean surface in the presence of two water molecules (*+2H₂O), which represent the reactants. Figure 10a illustrates the relative Gibbs free energy profiles of the elementary PCET. In addition, the side panels depict the corresponding overpotentials, which were evaluated on the basis of eq 16.

Among the surfaces evaluated, those derived from more oxidized iridium phases, especially IrO_2 , exhibit the lowest theoretical overpotentials. In particular, the more open $IrO_2(100)$ facet shows the most favorable energetic profile.

Interestingly, the terminations IrO_2 that exhibit the highest theoretical catalytic efficiency in this study are also frequently identified in experimental investigations as the preferentially exposed facets in practical OER catalysts. This correlation underscores the relevance of these surfaces not only in computational predictions but also in real-world applications, thus reinforcing the validity of the theoretical models employed. This enhanced performance can be attributed to a more balanced free energy distribution across the reaction intermediates, approaching the ideal scenario in which all PCET steps have similar thermodynamic levels. In contrast, the α -Ir₂O₃(10 $\overline{10}$) surface exhibits a significantly unbalanced energy profile, with more pronounced energetic mismatches between intermediates, indicating its limited catalytic efficiency.

The PDS varies among the investigated surfaces, primarily because of differences in the adsorption strength of key reaction intermediates. For Ir(100), Ir(111), and α -Ir₂O₃(0001), the third PCET step, namely, the formation of OOH* (eq 14), emerges as the PDS. In contrast, for $IrO_2(110)$, $IrO_2(100)$, and α - $Ir_2O_3(10\overline{10})$, the PDS corresponds to the fourth step, formation of O_2 (eq 15). This behavior is directly related to the adsorption free energies of O* and OOH*. Specifically, on those surfaces, $\Delta G_{\rm ad}^{\rm OOH}$ is highly negative, indicating strong OOH* binding. The pronounced magnitude creates a thermodynamic bottleneck in the OOH* \rightarrow O₂ step. In contrast, on surfaces such as Ir(100) and Ir(111), the relatively weaker adsorption of OOH* shifts the PDS to the O* \rightarrow OOH* step. For α -Ir₂O₃(1010), the pronounced structural instability of the surface, combined with overly strong adsorption of all OER intermediates, significantly inhibits the desorption of O2 as a gaseous product. This excessive binding energy results in a severe thermodynamic constraint, making the fourth PCET step the limiting step, thereby severely diminishing the overall catalytic efficiency of this surface for the OER.

The three reaction intermediates exhibit scaling relationships that have been widely discussed in previous studies. ^{74,75} Figure 10b illustrates that $\Delta G^*_{\rm OH}$ correlates positively with the variation in $\Delta G^*_{\rm OH}$ and this relationship is expressed by the linear fit $\Delta G_{\rm OOH} = 0.91 \Delta G_{\rm OH^*} + 2.96$ ($R^2 = 0.99$). This equation suggests a strong agreement with the expected linear coefficient range of 2.8–3.2 for oxides, ^{76,77} as commonly reported in the literature. The fact that our material class has a lower linear coefficient, closer to 2.8, further supports the notion that these materials are more conducive to the performance of the OER. Specifically, systems with a lower intercept tend to exhibit lower theoretical minimum overpotentials.

This scaling correlation between the intermediates can be explained through molecular orbital theory, which considers the electronic properties of the functional groups involved. Both intermediates interact with the catalytic surface primarily through the terminal oxygen, whose 2p orbitals overlap with the metal's d orbitals. These 2p orbitals form σ and $\sigma\pi$ bonding interactions with the metal's d orbitals. Consequently, the oxygen atom involved in adsorption is electronically similar to that of OH*, with the adsorbed OOH* molecule retaining similar electronic characteristics in its occupied and unoccupied orbital levels.⁷⁸ The extremes of the linear scaling are represented by Ir(111) and α -Ir₂O₃(0001), which, as a result, are the catalysts with the highest overpotentials.

These surfaces exhibit significant imbalances, either with very high values of $\Delta G_{\rm OH^*}$ and $\Delta G_{\rm OOH^*}$ (in the case of Ir(111) or very low values (as seen with $\alpha\text{-Ir}_2{\rm O}_3(0001)$. These disparities lead to high overpotentials, as the energy of $\Delta G_{\rm O^*}$ is balanced by the fixed energies of the reactants and products. In contrast, the surfaces IrO $_2(110)$ and IrO $_2(100)$ are positioned more proportionally and balanced, indicating that the energy variations of the reaction steps are more evenly distributed. In particular, IrO $_2(110)$ slightly deviates from the linear scaling trend, demonstrating that the OOH intermediate binds more weakly than expected, thus equalizing the energy levels of the OER steps. This leads to a lower overpotential as the reaction steps become more balanced.

The contour map presented in Figure 10c depicts a twodimensional volcano plot for the OER, where the catalytic performance is governed by two key thermodynamic descriptors: $\Delta G_{\text{OH}*}$ and $\Delta G_{\text{O}*}$. In this representation, the red regions correspond to highly active catalytic sites, while the blue areas indicate systems with elevated η^{OER} , and thus lower activity. By incorporating both descriptors simultaneously, this analysis enables a more comprehensive visualization of performance trends, highlighting regions where catalytic behavior approaches optimality. Importantly, this dualdescriptor framework enhances the interpretative scope compared to one-dimensional analyzes, particularly because $\Delta G_{
m OH^*}$ and $\Delta G_{
m OOH^*}$ are known to exhibit a strong linear correlation. As a result, the contribution of $\Delta G_{\mathrm{OOH}^*}$ can be indirectly inferred, allowing for a more informative and compact representation of the catalytic landscape.

Although the current set of materials does not provide a dense sampling sufficient to generate a continuous and well-resolved contour surface, meaningful distinctions between the different catalyst behaviors are still evident. In particular, the IrO₂ slabs are found to gather near $\Delta G_{\rm OH^*} \approx 0$, suggesting favorable adsorption energetics for the OH* intermediate. In contrast, systems such as Ir(111), Ir(100), and α -Ir₂O₃(0001) exhibit higher energy levels for the initial PCET step and a comparatively lower level for the second, resulting in a change in PDS to the third elementary step, namely O* \rightarrow OOH*. These materials tend to gather in the region associated with this PDS.

However, the α -Ir₂O₃(1010) facet shows a markedly different profile, with the first step highly exergonic and the second significantly below the ideal value. This suggests an overly strong binding of all intermediates, pointing to the fourth step, OOH* \rightarrow O₂, as surely PDS. Interestingly, for IrO₂ surfaces, the second reaction step exhibits values close to the ideal 1.23 eV, while the first step imposes the primary thermodynamic limitation. The strong adsorption of the OH* intermediate, reflected in its low free energy, results in a downward shift in energy levels on the Gibbs free energy, which ultimately limits the reduction of the overpotential.

Figure 11 provides a detailed examination of the Pourbaix diagram in proximity to the equilibrium lines, depicted as blue dashed lines, which illustrate the coexistence of H^+ - H_2 (top panel) and H_2O-O_2 (bottom panel). The colored lines represent the equilibrium positions of the adsorbed reaction intermediates for the HER (top panel) and OER (bottom panel), with the color scheme corresponding to each substrate as specified in the legend. The separation between the intermediate lines and the blue dashed line in the top panel denotes the overpotential necessary for HER. This observation

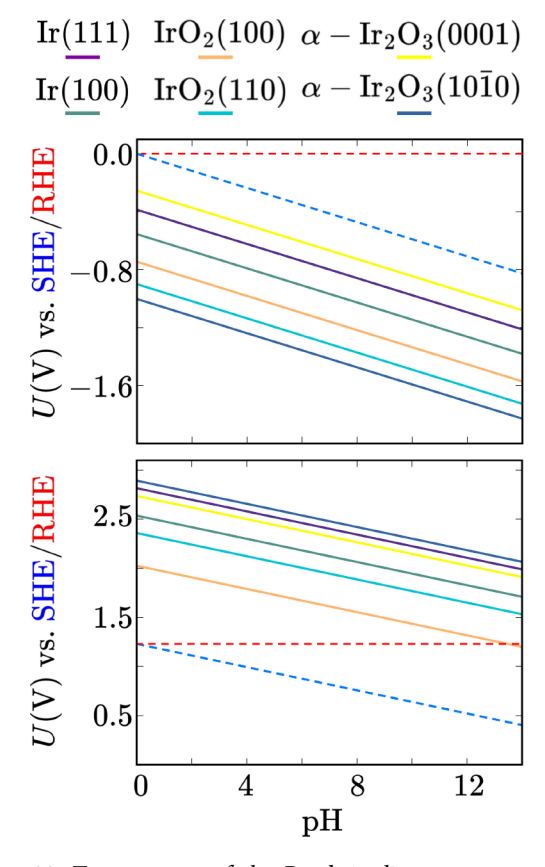


Figure 11. Two excerpts of the Pourbaix diagram are presented, highlighting the overall reactions of the HER (blue dashed line in the upper panel) and OER (blue dashed line in the lower panel) with respect to the SHE. Colored lines indicate the equilibrium of $H^* \rightarrow H_2$ (upper panel) or PDS equilibria of the OER intermediates (lower panel). The red dashed lines provide a comparison with the corresponding limits referenced to the reversible hydrogen electrode (RHE).

clearly indicates that α -Ir₂O₃(0001) and metallic Ir slabs demonstrate enhanced catalytic activity for HER.

In contrast, for OER, reference ${\rm IrO}_2$ illustrates that the PDS lines are in closest proximity to the overall reaction line as depicted in the bottom panel. In contrast, metallic Ir and references $\alpha\text{-Ir}_2{\rm O}_3$ exhibit PDS lines that are closely clustered, suggesting a comparatively less favorable behavior for the OER. Such findings are consistent with the trends observed in the volcano plot analysis, underscoring the relationship between overpotential and catalytic performance. Consequently, the diagram offers a lucid visual depiction of the relative efficiency of various Ir-based catalysts in both HER and OER.

4. CONCLUSIONS

In this study, a systematic computational study integrating density functional theory calculations with the computational hydrogen electrode model was conducted to elucidate the fundamental factors governing the distinct electronic, energetic, and catalytic properties of various iridium-based systems. By analyzing metallic Ir, rutile-type, and corundum-type oxide surfaces, we established definitive structure—property relationships that explain their differing electrocatalytic performances in the HER and OER reactions. This analysis offers fundamental insights into the influence of the atomic and electronic structures of iridium-based materials on

their catalytic efficiency, providing valuable guidance for the rational design of advanced electrocatalysts for water-splitting applications.

The results presented here reveal that higher oxidation states significantly impact the electronic structure and coordination environment of iridium, leading to pronounced variations in its thermodynamic stability. Metallic Ir exhibits high cohesive energy and compact atomic arrangement, which contributes to moderate activity toward HER. In contrast, the (0001) facet of α-Ir₂O₃, despite originating from a less stable bulk phase, reconstructs more effectively and emerges as the most promising surface termination among the investigated oxides to promote HER. On the other hand, the $(10\overline{10})$ facet displays a metallic-like character due to the loss of its initial semiconducting nature and exhibits excessively strong binding with reaction intermediates, ultimately impairing HER performance. This comparative analysis highlights the complex interaction between the oxidation state, surface coordination, and intermediate adsorption strength.

For the OER, the IrO₂ slabs exhibit the lowest overpotentials and the most favorable free energy profiles along the PCET pathway. These characteristics reflect a more balanced adsorption energy landscape, with intermediates interacting through a stronger Ir-O hybridization. Although the scaling relationships between adsorbed intermediates are confirmed and a specific region is identified in the two-dimensional descriptor space, where promising catalytic behavior can be anticipated, the key limitation remains the intrinsically high adsorption energy of certain intermediates, particularly OH^* . This strongly bound intermediate establishes a fundamental bottleneck in the catalytic performance of this class of materials. Therefore, by integrating geometrical and electronic structure insights with thermodynamic descriptors, this study delineates a strategic framework for future investigations aimed at fine-tuning such interactions. In this context, subsequent studies may focus on the incorporation of dopants or the introduction of surface defects as rational approaches to modulate the electronic environment and adsorption strength, ultimately guiding the design of more efficient HER/OER catalysts.

ASSOCIATED CONTENT

Data Availability Statement

As mentioned, all DFT calculations were done using the VASP version 5.4.4 package, which can be used under a nonfree academic license. Additional details can be obtained from the link, https://www.vasp.at/. Furthermore, additional details are provided within the electronic Supporting Information, while additional crude data can be obtained directly with the authors upon request.

Supporting Information

The Supporting Information is available free of charge at https://pubs.acs.org/doi/10.1021/acsaem.5c02853.

Computational parameters; convergence tests; adsorption energies and geometries; Gibbs free-energy calculations for HER and OER; DOS and charge density analyses; bulk and gas-phase molecular data; CHE model details; supplementary tables and figures; and the data used for the figures, as well as complementary analyses and additional technical details (Electronic Supporting Information (ESI)) (PDF)

AUTHOR INFORMATION

Corresponding Author

Juarez L. F. Da Silva — São Carlos Institute of Chemistry, University of São Paulo, 13560-970 Sao Carlos, SP, Brazil; o orcid.org/0000-0003-0645-8760; Email: juarez dasilva@iqsc.usp.br

Authors

Marionir M. C. B. Neto — São Carlos Institute of Chemistry, University of São Paulo, 13560-970 Sao Carlos, SP, Brazil Pedro Ivo R. Moraes — São Carlos Institute of Chemistry, University of São Paulo, 13560-970 Sao Carlos, SP, Brazil; orcid.org/0000-0001-7339-5945

Complete contact information is available at: https://pubs.acs.org/10.1021/acsaem.5c02853

Funding

The Article Processing Charge for the publication of this research was funded by the Coordenacao de Aperfeicoamento de Pessoal de Nivel Superior (CAPES), Brazil (ROR identifier: 00x0ma614).

Notes

The authors declare no competing financial interest.

ACKNOWLEDGMENTS

The authors gratefully acknowledge support from FAPESP (São Paulo Research Foundation) and Shell, projects No. 2017/11631-2 and 2018/21401-7, and the strategic importance of the support given by ANP (Brazil's National Oil, Natural Gas and Biofuels Agency) through the R&D levy regulation. PIRM acknowledges financial support (Postdoctoral fellowship) from FAPESP, project No. 2023/12824-0. The authors also thank the infrastructure provided to our computer cluster by the Department of Information Technology—Campus São Carlos. The research was developed with the help of HPC resources provided by the Information Technology Superintendence of the University of São Paulo. We acknowledge the use of advanced language models for their assistance in English-language editing, grammar revision, and text refinement.

ABBREVIATIONS

DFT density functional theory PBE Perdew-Burke-Ernzerhof

VASP Vienna ab initio simulation package

HER hydrogen evolution reaction OER oxygen evolution reaction

CHE computational hydrogen electrode

PDS potential determining step

PCET proton-coupled electron transfer

REFERENCES

- (1) Guilbert, D.; Vitale, G. Hydrogen as a Clean and Sustainable Energy Vector for Global Transition from Fossil-Based to Zero-Carbon. *Clean Technol.* **2021**, *3*, 881–909.
- (2) He, G.; Mallapragada, D. S.; Bose, A.; Heuberger-Austin, C. F.; Gençer, E. Sector Coupling via Hydrogen to Lower the Cost of Energy System Decarbonization. *Energy Environ. Sci.* **2021**, *14*, 4635–4646.
- (3) Cevik, S. Climate Change and Energy Security: the Dilemma or Opportunity of the Century? *Econ. Env. Polym.* **2024**, *26*, 653–672.

- (4) Fei, L.; Sun, H.; Li, Y.; Gu, Y.; Zhou, W.; Shao, Z. Recent Advances in Innovative Systems for Electrocatalytic Hydrogen Production. *Energy Environ. Sci.* **2025**, *493*, No. 144933.
- (5) Miao, L.; Jia, W.; Cao, X.; Jiao, L. Computational Chemistry for Water-Splitting Electrocatalysis. *Chem. Soc. Rev.* **2024**, *53*, 2771–2807.
- (6) Karfa, P.; Majhi, K. C.; Madhuri, R. Shape-Dependent Electrocatalytic Activity of Iridium Oxide Decorated Erbium Pyrosilicate Toward the Hydrogen Evolution Reaction Over the Entire pH Range. ACS Catal. 2018, 8, 8830–8843.
- (7) Kronberg, R.; Laasonen, K. Reconciling the Experimental and Computational Hydrogen Evolution Activities of Pt(111) through DFT-Based Constrained MD Simulations. ACS Catal. 2021, 11, 8062–8078.
- (8) Tang, L.; Chen, X.; Xie, Z.; Xiang, Q.; Liu, J.; Li, L.; Wei, Z. Metal—oxygen bonding characteristics dictate activity and stability differences of RuO₂ and IrO₂ in the Acidic Oxygen Evolution Reaction. *Phys. Chem. Chem. Phys.* **2025**, *27*, 9369–9378.
- (9) Zagalskaya, A.; Alexandrov, V. Mechanistic Study of IrO₂ Dissolution During the Electrocatalytic Oxygen Evolution Reaction. *J. Phys. Chem. Lett.* **2020**, *11*, 2695–2700.
- (10) McCrory, C. C.; Jung, S.; Ferrer, I. M.; Chatman, S. M.; Peters, J. C.; Jaramillo, T. F. Benchmarking Hydrogen Evolving Reaction and Oxygen Evolving Reaction Electrocatalysts for Solar Water Splitting Devices. J. Am. Chem. Soc. 2015, 137, 4347–4357.
- (11) Wang, C.; Lan, F.; He, Z.; Xie, X.; Zhao, Y.; Hou, H.; Guo, L.; Murugadoss, V.; Liu, H.; Shao, Q. others Iridium-Based Catalysts for Solid Polymer Electrolyte Electrocatalytic Water Splitting. *Chem. Sus. Chem.* **2019**, *12*, 1576–1590.
- (12) Jiang, B.; Wang, T.; Cheng, Y.; Liao, F.; Wu, K.; Shao, M. Ir/g-C3N4/Nitrogen-Doped Graphene Nanocomposites as Bifunctional Electrocatalysts for Overall Water Splitting in Acidic Electrolytes. *ACS Appl. Mater. Interfaces* **2018**, *10*, 39161–39167.
- (13) Kim, S.-j.; Jung, H.; Lee, C.; Kim, M. H.; Lee, Y. Comparative Study on Hydrogen Evolution Reaction Activity of Electrospun Nanofibers with Diverse Metallic Ir and IrO₂ Composition Ratios. *ACS Sustain. Chem. Eng.* **2019**, *7*, 8613–8620.
- (14) Pfeifer, V.; Jones, T.; Vélez, J. V.; Massué, C.; Greiner, M.; Arrigo, R.; Teschner, D.; Girgsdies, F.; Scherzer, M.; Allan, J. others The Electronic Structure of Iridium Oxide Electrodes Active in Water Splitting. *Phys. Chem. Chem. Phys.* **2016**, *18*, 2292–2296.
- (15) Kawar, R.; Chigare, P.; Patil, P. Substrate Temperature Dependent Structural, Optical and Electrical Properties of Spray Deposited Iridium Oxide Thin Films. *Appl. Surf. Sci.* **2003**, *206*, 90–101.
- (16) Kan, S.-i.; Takemoto, S.; Kaneko, K.; Takahashi, I.; Sugimoto, M.; Shinohe, T.; Fujita, S. Electrical Properties of α -Ir₂O₃/ α -Ga₂O₃ pn Heterojunction Diode and Band Alignment of the Heterostructure. *Appl. Phys. Lett.* **2018**, *113*, .
- (17) Zhao, Z.-J.; Gong, J. Uncertainties in Theoretical Description of Well-Defined Heterogeneous Catalysts. *Stud. Surf. Sci. Catal.* **2017**, 177, 541–565.
- (18) Kresse, G.; Furthmüller, J. Efficient Iterative Schemes for Ab initio Total-energy Calculations Using a Plane-wave Basis set. *Phys. Rev. B* **1996**, *54*, 11169–11186.
- (19) Kresse, G.; Joubert, D. From Ultrasoft Pseudopotentials to the Projector Augmented-wave Method. *Phys. Rev. B* **1999**, *59*, 1758–1775.
- (20) Blöchl, P. E. Projector Augmented-Wave Method. *Phys. Rev. B* **1994**, *50*, 17953–17979.
- (21) Perdew, J. P.; Burke, K.; Ernzerhof, M. Generalized Gradient Approximation Made Simple. *Phys. Rev. Lett.* **1996**, *77*, 3865–3868.
- (22) Tereshchuk, P.; Amaral, R. C.; Seminovski, Y.; Da Silva, J. L. F. Glycerol Adsorption on a Defected Pt6/Pt(100) Substrate: A Density Functional Theory Investigation Within the D3 van der Waals Correction. RSC Adv. 2017, 7, 17122–17127.
- (23) Neto, M. M.; Verga, L. G.; Da Silva, J. L.; Galvão, B. R. Computational Screening of Silver-Based Single-Atom Alloys Catalysts for CO₂ Reduction. *J. Chem. Phys.* **2024**, *160*, .

- (24) Grimme, S.; Antony, J.; Ehrlich, S.; Krieg, H. A Consistent and Accurate ab Initio Parametrization of Density Functional Dispersion Correction (DFT-D) for the 94 Elements H-Pu. *J. Chem. Phys.* **2010**, 132, 154104.
- (25) Monkhorst, H. J.; Pack, J. D. Special Points for Brillouin-zone Integrations. *Phys. Rev. B* **1976**, *13*, 5188–5192.
- (26) Nørskov, J. K.; Rossmeisl, J.; Logadottir, A.; Lindqvist, L.; Kitchin, J. R.; Bligaard, T.; Jónsson, H. Origin of the Overpotential for Oxygen Reduction at a Fuel-cell Cathode. *J. Phys. Chem. B* **2004**, *108*, 17886–17892.
- (27) Peterson, A. A.; Abild-Pedersen, F.; Studt, F.; Rossmeisl, J.; Nørskov, J. K. How Copper Catalyzes the Electroreduction of Carbon Dioxide Into Hydrocarbon Fuels. *Energy Environ. Sci.* **2010**, *3*, 1311.
- (28) Larsen, A. H.; Mortensen, J. J.; Blomqvist, J.; Castelli, I. E.; Christensen, R.; Dułak, M.; Friis, J.; Groves, M. N.; Hammer, B.; Hargus, C. others The Atomic Simulation Environment—a Python Library for Working with Atoms. *J. Condens. Matter Phys.* **2017**, 29, 273002–273032.
- (29) Inico, E.; Di Liberto, G.; Giordano, L. Stability and Solvation of Key Intermediates of Oxygen Evolution on TiO₂, RuO₂, IrO₂(110) Surfaces: A Comparative DFT Study. *Chem. Catal. Chem.* **2024**, *16*, No. e202400813.
- (30) Sabatier, P. Hydrogénations et Déshydrogénations par Catalyse. *Ber. dtsch. chem. Ges.* **1911**, 44, 1984–2001.
- (31) Fabbri, E.; Habereder, A.; Waltar, K.; Kötz, R.; Schmidt, T. J. Developments and Perspectives of Oxide-Based Catalysts for the Oxygen Evolution Reaction. *Catal. Sci. Technol.* **2014**, *4*, 3800–3821.
- (32) Zhang, X.; Bieberle-Hütter, A. Modeling and Simulations in Photoelectrochemical Water Oxidation: from Single Level to Multiscale Modeling. *Chem. Sus. Chem.* **2016**, *9*, 1223–1242.
- (33) Zhang, K.; Zou, R. Advanced Transition Metal-Based OER Electrocatalysts: Current Status, Opportunities, and Challenges. *Small* **2021**, *17*, 2100129.
- (34) Sargeant, E.; Illas, F.; Rodriguez, P.; Calle-Vallejo, F. Importance of the Gas-Phase Error Correction for O₂ When Using DFT to Model the Oxygen Reduction and Evolution Reactions. *J. Electroanal. Chem.* **2021**, *896*, No. 115178.
- (35) Liang, Q.; Brocks, G.; Bieberle-Hütter, A. Oxygen Evolution Reaction (OER) Mechanism Under Alkaline and Acidic Conditions. *J. Phys. E* **2021**, *3*, No. 026001.
- (36) Alia, S. M.; Ha, M.-A.; Anderson, G. C.; Ngo, C.; Pylypenko, S.; Larsen, R. E. The Roles of Oxide Growth and Sub-Surface Facets in Oxygen Evolution Activity of Iridium and Its Impact on Electrolysis. *J. Electrochem. Soc.* **2019**, *166*, F1243.
- (37) Murawski, J.; Scott, S. B.; Rao, R.; Rigg, K.; Zalities, C.; Stevens, J.; Sharman, J.; Hinds, G.; Stephens, I. E. Benchmarking Stability of Iridium Oxide in Acidic Media Under Oxygen Evolution Conditions: a Review Part 1. *Johns. Matthey Technol. Rev.* **2024**, *68*, 121–146.
- (38) Qin, X.; Zhu, S.; Wang, Y.; Pan, D.; Shao, M. Full Atomistic Mechanism Study of Hydrogen Evolution Reaction on Pt Surfaces at Universal pHs: Ab initio Simulations at Electrochemical Interfaces. *Electrochim. Acta* **2022**, *425*, No. 140709.
- (39) Sinha, V.; Sun, D.; Meijer, E.; Vlugt, T.; Bieberle-Hütter, A. A Multiscale Modelling Approach to Elucidate the Mechanism of the Oxygen Evolution Reaction at the Hematite-Water Interface. *Faraday Discuss.* **2021**, 229, 89–107.
- (40) Liu, C.; Zhu, L.; Ren, P.; Wen, X.; Li, Y.-W.; Jiao, H. High-Coverage CO Adsorption and Dissociation on Ir(111), Ir(100), and Ir(110) from Computations. *J. Phys. Chem. C* **2019**, *123*, 6487–6495.
- (41) Matz, O.; Calatayud, M. Periodic DFT Study of Rutile IrO₂: Surface Reactivity and Catechol Adsorption. *J. Phys. Chem. C* **2017**, 121, 13135–13143.
- (42) He, Y.; Stierle, A.; Li, W.; Farkas, A.; Kasper, N.; Over, H. Oxidation of Ir(111): From O- Ir- O Trilayer to Bulk Oxide Formation. *J. Phys. Chem. C* **2008**, *112*, 11946–11953.
- (43) Alexandrov, V.; Piskunov, S.; Zhukovskii, Y. F.; Kotomin, E. A.; Maier, J. First-Principles Modeling of Oxygen Interaction with

- SrTiO₃(001) Surface: Comparative Density-Functional LCAO and Plane-Wave Study. *Integr. Ferroelectr.* **2011**, 123, 10–17.
- (44) Hoppe, R. Effective Coordination Numbers (ECoN) and Mean Active Fictive Ionic Radii (MEFIR). Z. Kristallogr. 1979, 150, 23-52.
- (45) Da Silva, J. L. F. Effective Coordination Concept Applied for Phase Change (GeTe)·m(Sb2Te3)·n Compounds. *J. Appl. Phys.* **2011**, *109*, No. 023502.
- (46) Al-Mahayni, H.; Wang, X.; Harvey, J.-P.; Patience, G. S.; Seifitokaldani, A. Experimental Methods in Chemical Engineering: Density Functional Theory. *Can. J. Chem. Eng.* **2021**, *99*, 1885–1911.
- (47) Bader, R. F. W. Atoms in Molecules: A Quantum Theory; In International Series of Monographs on Chemistry; Clarendon Press, 1994
- (48) Henkelman, G.; Arnaldsson, A.; Jónsson, H. A Fast and Robust Algorithm for Bader Decomposition of Charge Density. *Comput. Mater. Sci.* **2006**, *36*, 354–360.
- (49) Shannon, R. D. Revised Effective Ionic Radii and Systematic Studies of Interatomic Distances in Halides and Chalcogenides. *Acta Crystallogr., Sect. A: Found. Crystallogr.* **1976**, 32, 751–767.
- (50) Owen, E.; Yates, E. XLI. Precision Measurements of Crystal Parameters. London Edinb. Dublin Philos. Mag. J. Sci. 1933, 15, 472–488.
- (51) Bestaoui, N.; Prouzet, E.; Deniard, P.; Brec, R. Structural and Analytical Characterization of an Iridium Oxide Thin Layer. *Thin Solid Films.* **1993**, 235, 35–42.
- (52) Chung, W.-H.; Tsai, D.-S.; Fan, L.-J.; Yang, Y.-W.; Huang, Y.-S. Surface Oxides of Ir(111) Prepared by Gas-Phase Oxygen Atoms. Surf. Sci. 2012, 606, 1965–1971.
- (53) Khalid, S.; Janotti, A. Electronic Properties of Corundum-Like Ir₂O₃ and Ir₂O₃-Ga₂O₃ alloys. *Appl. Phys. Lett.* **2024**, *125*, 114451.
- (54) Ping, Y.; Galli, G.; Goddard, W. A., III Electronic Structure of IrO_2 : the Role of the Metal d Orbitals. J. Phys. Chem. C **2015**, 119, 11570–11577.
- (55) Phillips, J. Ionicity of the Chemical Bond in Crystals. *J. Appl. Phys.* **1970**, 42, 317–356.
- (56) Kittel, C. Introduction to Solid State Physics, 8th ed.; John Wiley & Sons, Inc.: New York, 2004.
- (57) Michaelson, H. B. The Work Function of the Elements and its Periodicity. *J. Appl. Phys.* **1977**, *48*, 4729–4733.
- (58) Wang, J.; Wang, S.-Q. Surface Energy and Work Function of FCC and BCC Crystals: Density Functional Study. *Surf. Sci.* **2014**, 630, 216–224.
- (59) Yeh, C.-H.; Pham, T. M. L.; Nachimuthu, S.; Jiang, J.-C. Effect of External Electric Field on Methane Conversion on $IrO_2(110)$ Surface: a Density Functional Theory Study. *ACS Catal.* **2019**, *9*, 8230–8242.
- (60) Papaconstantopoulos, D. A.; Handbook of the Band Structure of Elemental Solids; Springer, 1986; .
- (61) Hammer, B.; Nørskov, J. K. Electronic Factors Determining the Reactivity of Metal Surfaces. *Surf. Sci.* **1995**, 343, 211–220.
- (62) Chen, H.; Dawson, J. A.; Umezawa, N. Anisotropic Nature of Anatase ${\rm TiO_2}$ and Its Intrinsic (001) Surface Electronic States. *Phys. Rev. Appl.* **2015**, *4*, No. 014007.
- (63) Ovcharenko, R.; Voloshina, E.; Sauer, J. Water Adsorption and O-Defect Formation on Fe₂O₃(0001) surfaces. *Phys. Chem. Chem. Phys.* **2016**, *18*, 25560–25568.
- (64) Klyukin, K.; Zagalskaya, A.; Alexandrov, V. Ab initio Thermodynamics of Iridium Surface Oxidation and Oxygen Evolution Reaction. *J. Phys. Chem. C* **2018**, *122*, 29350–29358.
- (65) Freire, R. L. H.; Orlandi, M. O.; Da Silva, J. L. F. Ab initio Investigation of the Role of Charge Transfer in the Adsorption Properties of H₂, N₂, O₂, CO, NO, CO₂, NO₂, and CH₄ on the van der Waals Layered Sn3O4 Semiconductor. *Phys. Rev. Mater.* **2020**, *4*, .
- (66) Zhang, H.; Li, W.-X. First-principles Investigation of Surface and Subsurface H Adsorption on Ir(111). *J. Phys. Chem. C* **2009**, *113*, 21361–21367.
- (67) Lerch, D.; Klein, A.; Schmidt, A.; Müller, S.; Hammer, L.; Heinz, K.; Weinert, M. Unusual Adsorption Site of Hydrogen on the Unreconstructed Ir(100) surface. *Phys. Rev. B* **2006**, *73*, No. 075430.

- (68) Lewis, R.; Gomer, R. Adsorption of Hydrogen on Platinum. *Surf. Sci.* **1969**, *17*, 333–345.
- (69) Pistonesi, C.; Pronsato, E.; Juan, A. A DFT study of H adsorption on Pt(111) and Pt-Ru(111) Surfaces. *Appl. Surf. Sci.* **2008**, 254, 5827–5830.
- (70) Schnur, S.; Groß, A. Strain and Coordination Effects in the Adsorption Properties of Early Transition Metals: A Density-Functional Theory Study. *Phys. Rev. B* **2010**, *81*, No. 033402.
- (71) Galimberti, D. R.; Sauer, J. Chemically Accurate Vibrational Free Energies of Adsorption from Density Functional Theory Molecular Dynamics: Alkanes in Zeolites. *J. Chem. Theory Comput.* **2021**, *17*, 5849–5862.
- (72) Zhang, J.; Zhang, L.; Liu, J.; Zhong, C.; Tu, Y.; Li, P.; Du, L.; Chen, S.; Cui, Z. OH Spectator at IrMo Intermetallic Narrowing Activity Gap Between Alkaline and Acidic Hydrogen Evolution Reaction. *Nat. Commun.* **2022**, *13*, 5497–5505.
- (73) Fratarcangeli, M.; Vigil, S. A.; Lin, Z.; Soderstedt, C. J.; Moreno-Hernandez, I. A. Direct Observation of Structural Disorder Effects on Iridium Dioxide Nanocrystal Dissolution. *Matter.* **2025**, *8*, 101909
- (74) Man, I. C.; Su, H.-Y.; Calle-Vallejo, F.; Hansen, H. A.; Martínez, J. I.; Inoglu, N. G.; Kitchin, J.; Jaramillo, T. F.; Nørskov, J. K.; Rossmeisl, J. Universality in Oxygen Evolution Electrocatalysis on Oxide Surfaces. *Chem. Catal. Chem.* **2011**, *3*, 1159–1165.
- (75) Viswanathan, V.; Hansen, H. A.; Rossmeisl, J.; Nørskov, J. K. Universality in Oxygen Reduction Electrocatalysis on Metal Surfaces. *ACS Catal.* **2012**, *2*, 1654–1660.
- (76) Calle-Vallejo, F.; Martínez, J.; García-Lastra, J.; Abad, E.; Koper, M. Oxygen Reduction and Evolution at Single-Metal Active Sites: Comparison Between Functionalized Graphitic Materials and Protoporphyrins. *Surf. Sci.* **2013**, *607*, 47–53.
- (77) Viswanathan, V.; Hansen, H. A. Unifying Solution and Surface Electrochemistry: Limitations and Opportunities in Surface Electrocatalysis. *Top. Catal.* **2014**, *57*, 215–221.
- (78) Fang, C.; Zhou, J.; Zhang, L.; Wan, W.; Ding, Y.; Sun, X. Synergy of Dual-Atom Catalysts Deviated from the Scaling Relationship for Oxygen Evolution Reaction. *Nat. Commun.* **2023**, *14*, 4449.

